

Field-induced electronic correlations and superconductivity in UTe_2 beyond 40 T

T. Thebault,¹ K. Somesh,¹ G. Lapertot,² M. Nardone,¹ A. Zitouni,¹ M. Barragan,¹ J. Béard,¹ J. Billette,¹ F. Lecouturier,¹ S. Tardieu,¹ D. Aoki,³ G. Knebel,² D. Braithwaite,² and W. Knafo¹

¹*Laboratoire National des Champs Magnétiques Intenses - EMFL, CNRS, Univ. Grenoble Alpes, INSA-T, Univ. Toulouse 3, 31400 Toulouse, France*

²*Univ. Grenoble Alpes, CEA, Grenoble INP, IRIG, PHELIQS, 38000, Grenoble, France*

³*Institute for Materials Research, Tohoku University, Ikaraki 311-1313, Japan*

(Dated: May 15, 2025)

Several superconducting phases have been discovered close to a metamagnetic transition in the heavy-fermion compound UTe_2 , unveiling a close relation between its superconducting and magnetic properties. Although suspected to be of magnetic nature, the mechanisms stabilizing these superconducting phases remain mysterious. Here, we present electrical-resistivity measurements on UTe_2 , with a current $\mathbf{I} \parallel \mathbf{a}$ and under pulsed magnetic fields up to 60 T rotating in the (\mathbf{b}, \mathbf{c}) plane. The Fermi-liquid coefficient A of the electrical resistivity reaches its maximal values at the metamagnetic transition in fields tilted by $30 - 40^\circ$ from \mathbf{b} to \mathbf{c} , and it becomes asymmetric with higher values above the metamagnetic field than below. The enhancement of A is interpreted as resulting from enhanced magnetic fluctuations, in a regime which coincides with a domain of stabilization of superconductivity beyond 40 T. These results show that the magnetic fluctuations probed here probably play a key role in stabilizing high-field superconductivity in UTe_2 and may provide further insight into the superconducting mechanisms.

In heavy-fermion systems, magnetic fluctuations have often been identified as responsible for the appearance of unconventional superconductivity [1]. A Fermi-liquid behavior associated with large effective masses of quasi-particles is observed and a relation between the strength of magnetic fluctuations and the amplitude of the effective mass has been emphasized [2]. One can indirectly characterize the evolution of the magnetic-fluctuations strength, as function of a tuning parameter, as pressure or magnetic field, by studying the Fermi-liquid coefficients extracted from thermodynamic experiments, as the Sommerfeld heat-capacity coefficient γ , or from transport measurements, as the electrical-resistivity coefficient A . In the last two decades, magnetic-field-induced superconductivity in the uranium-based heavy-fermion ferromagnets URhGe , UCoGe , and UGe_2 has attracted considerable attention [3]. In these systems, a superconducting phase is induced or reinforced in a magnetic field and develops in the vicinity of a metamagnetic transition, at which ferromagnetic fluctuations are suspected to be involved in the superconducting pairing mechanism [4, 5]. In URhGe , an enhancement of the Fermi-liquid electrical-resistivity coefficient A at the metamagnetic transition, in the vicinity of a field-induced superconducting phase, was proposed to result from ferromagnetic fluctuations [6–8]. The presence of magnetic fluctuations at the metamagnetic transition was supported by nuclear-magnetic-resonance (NMR) relaxation-rate studies [9, 10]. More recently, several field-induced superconducting phases have been discovered in the paramagnetic heavy-fermion compound UTe_2 , revealing a new playground to study the relation between magnetism and superconductivity [11–17]. At zero magnetic field, a superconducting phase SC1 is stabilized below $T_{sc} \approx 2$ K

and was identified as a candidate for a triplet mechanism [18–21]. Antiferromagnetic fluctuations are developing at low temperature [22–26] and UTe_2 is located near an antiferromagnetic instability, as shown by the onset of long-range antiferromagnetic order under pressure [27]. NMR Knight-shift experiments confirmed the presence of magnetic fluctuations at low temperatures [28–30].

By applying a magnetic field to UTe_2 along its crystallographic direction \mathbf{b} , SC1 vanishes near 20 T and a field-induced superconducting phase SC2 is stabilized for $20 \text{ T} \lesssim H \lesssim H_m$, near a metamagnetic transition at $\mu_0 H_m = 34 \text{ T}$, the transition temperature of SC2 being maximum near H_m [11, 12, 31–33]. By tilting the magnetic field from \mathbf{b} to \mathbf{c} , a second field-induced superconducting phase SC-PPM is stabilized for $H \gtrsim H_m$ in the vicinity of the metamagnetic transition observed then at $\mu_0 H_m = 40 - 45 \text{ T}$ [11, 34, 35]. The metamagnetic field H_m and the boundaries of SC2 and SC-PPM were mapped out as function of the three components of the magnetic-field direction, showing a complex three-dimensional phase diagram [15, 16, 36]. The Fermi-liquid Sommerfeld coefficient γ in the heat capacity and the quadratic coefficient A in the electrical resistivity of UTe_2 were shown to exhibit a maximum at the metamagnetic transition for the two field directions $\mathbf{H} \parallel \mathbf{b}$ and \mathbf{H} tilted by 30° from \mathbf{b} to \mathbf{c} [31, 33, 34, 37–39]. For $\mathbf{H} \parallel \mathbf{b}$, a similar magnetic-field variation of the NMR relaxation rates and A (measured with an electrical current $\mathbf{I} \parallel \mathbf{a}$) was found, supporting that the Fermi-liquid regime is controlled by the magnetic fluctuations [40] and, thus, that their intensity is maximum at the metamagnetic transition. However, the reasons for the different domains of stability of SC2 and SC-PPM remain mysterious. A systematic characterization of the magnetic fluctuations

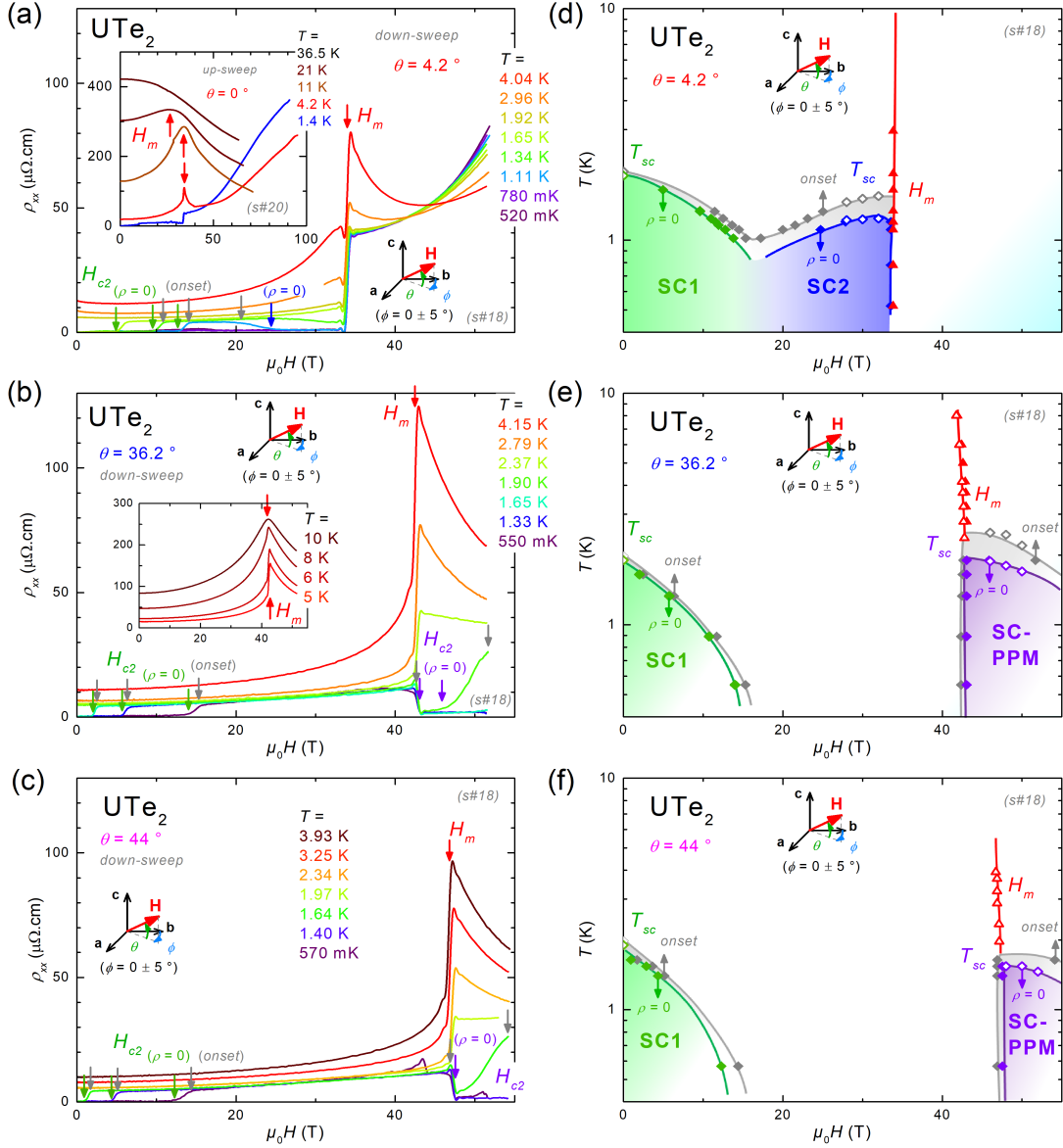


FIG. 1. Left-hand graphs: Electrical resistivity ρ_{xx} of UTe_2 versus magnetic field up to 55 T, at temperatures T from 500 mK to 36.5 K, for field directions with the angles $\theta = (\mathbf{b}, \mathbf{H}) =$ (a) 4.2° , (b) 36.2° , and (c) 44° . The data in the main Panels and in the Inset of Panel (b) were obtained on sample #18 during the fall of pulsed magnetic fields up to 55 T, and the data in the Inset of Panel (a) were obtained on sample #20 during the rise of pulsed magnetic fields up to 95 T. Right-hand graphs: Magnetic-field-temperature phase diagrams obtained for $\theta =$ (d) 4.2° , (e) 36.2° , and (f) 44° . In the phase diagrams, the open symbols correspond to points extracted from $\rho_{xx}(T)$ data and closed symbols correspond to points extracted from $\rho_{xx}(H)$ data.

developing near the metamagnetic transition, under high magnetic fields rotating in the (\mathbf{b}, \mathbf{c}) plane, is now needed to address this question.

In this letter, we present electrical-resistivity measurements on UTe_2 single crystals in magnetic fields applied in the (\mathbf{b}, \mathbf{c}) plane. Different samples (labeled #16, #18, #19, and #20; see details in the Supplemental Material [41]) grown by the molten-salt-flux (MSF) method [42] have been studied. The electrical resistivity ρ_{xx} has been measured by the four-point method with a current

$\mathbf{I} \parallel \mathbf{a}$. Magnetic fields have been generated by long-duration pulsed magnets at the Laboratoire National des Champs Magnétiques Intenses in Toulouse. A standard single-coil magnet has been used for most of the measurements presented here, which were done in magnetic fields up to 55 T and temperatures from 500 mK to 10 K delivered by a 10-mm bore ^3He insert. A triple-coil prototype was used to generate magnetic fields up to 95 T (see [43]), at temperatures from 1.4 to 36.5 K delivered by a 4-mm bore ^4He cryostat, for complementary mea-

measurements. We extract the magnetic-field evolution of the Fermi-liquid coefficient A and of the superconducting temperatures T_{SC2} and T_{SC-PPM} of the phases SC2 and SC-PPM, respectively, for field angles $\theta = (\mathbf{b}, \mathbf{H})$ varying from 4.2 to 44°. Our data show signatures from enhanced magnetic fluctuations in the vicinity of the magnetic-field-induced superconducting phase SC-PPM, which supports that these magnetic fluctuations may play a role in the mechanism driving SC-PPM.

The electrical resistivity ρ_{xx} measured in magnetic fields with the angles $\theta = 4.2$, 36.2 and 44° and temperatures from $T = 500$ mK to 10 K is presented in Figs. 1(a-c). At $\theta = 4.2^\circ$, SC2 is stabilized in the field window $15 \text{ T} < \mu_0 H < \mu_0 H_m \simeq 34 \text{ T}$, at temperatures $T \leq 1.2 \text{ K}$ [Fig. 1(a)]. At temperatures $T \leq 6 \text{ K}$, a sharp step-like increase of the resistivity occurs at the metamagnetic field H_m . At temperatures $T > 6 \text{ K}$, the metamagnetic transition is transformed into a crossover characterized by a broad maximum in ρ_{xx} , as observed in previous studies [31, 34]. An increase of the resistivity ρ_{xx} is observed at high fields and low temperatures, from $\simeq 45 \mu\Omega\text{cm}$ at $\mu_0 H = 45 \text{ T}$ to $\simeq 350 \mu\Omega\text{cm}$ at $\mu_0 H = 95 \text{ T}$ at the temperature $T = 1.4 \text{ K}$ [see Inset of Fig. 1(a)]. Knowing that UTe_2 is a compensated metal [44], this increase of ρ_{xx} is attributed to the cyclotron motion of the conduction electrons in a transverse configuration (current orthogonal to the magnetic field) [45]. A similar behavior was already observed in the electrical resistivity of UTe_2 with electrical currents $\mathbf{I} \parallel \mathbf{a}, \mathbf{c}$ under a magnetic field $\mathbf{H} \parallel \mathbf{b}$ [31, 39]. For $\theta = 36.2$ and 44°, the superconducting phase SC-PPM is stabilized for $H > H_m$ with $\mu_0 H_m = 43 \text{ T}$ and 47.5 T, respectively [Figs. 1(b-c)]. No cyclotron-motion effect is observed in fields up to 60 T applied along these directions. In the vicinity of H_m , the temperature variation of the electrical resistivity is the largest for $\theta = 36.2^\circ$. Magnetic-field-temperature phase diagrams obtained from our electrical-resistivity measurements are presented in Figs. 1(d-f). For $\theta = 4.2^\circ$, the highest critical temperature $T_{SC2}^{max} = 1.25 \text{ K}$ of SC2 is found at $\mu_0 H \approx 32 \text{ T}$, i.e., just below H_m [Fig. 1(d)]. For $\theta = 36.2$ and 44°, the critical temperature of SC-PPM is maximum in fields just above the metamagnetic field, where it reaches $T_{SC-PPM}^{max} = 1.9 \text{ K}$ and 1.55 K, respectively [Figs. 1(e-f)].

The electrical resistivity ρ_{xx} measured at $T = 4 \pm 0.15 \text{ K}$ in magnetic fields with angles θ varying from 4.2° to 44.4° is presented in Fig. 2(a). ρ_{xx} is maximum at the metamagnetic transition and its maximum is enhanced at angles $28.5 \leq \theta \leq 36.2^\circ$, where it reaches $\simeq 120 \mu\Omega\text{cm}$ and where the largest resistivity jump $\Delta\rho(H_m) \simeq 70 \mu\Omega\text{cm}$ is observed at H_m . Fig. 2(b) shows the magnetic-field dependence of the Fermi-liquid coefficient A extracted from our data. Details about the Fermi-liquid fits to the electrical-resistivity data, by $\rho_{xx} = \rho_0 + AT^2$, are given in the Supplemen-

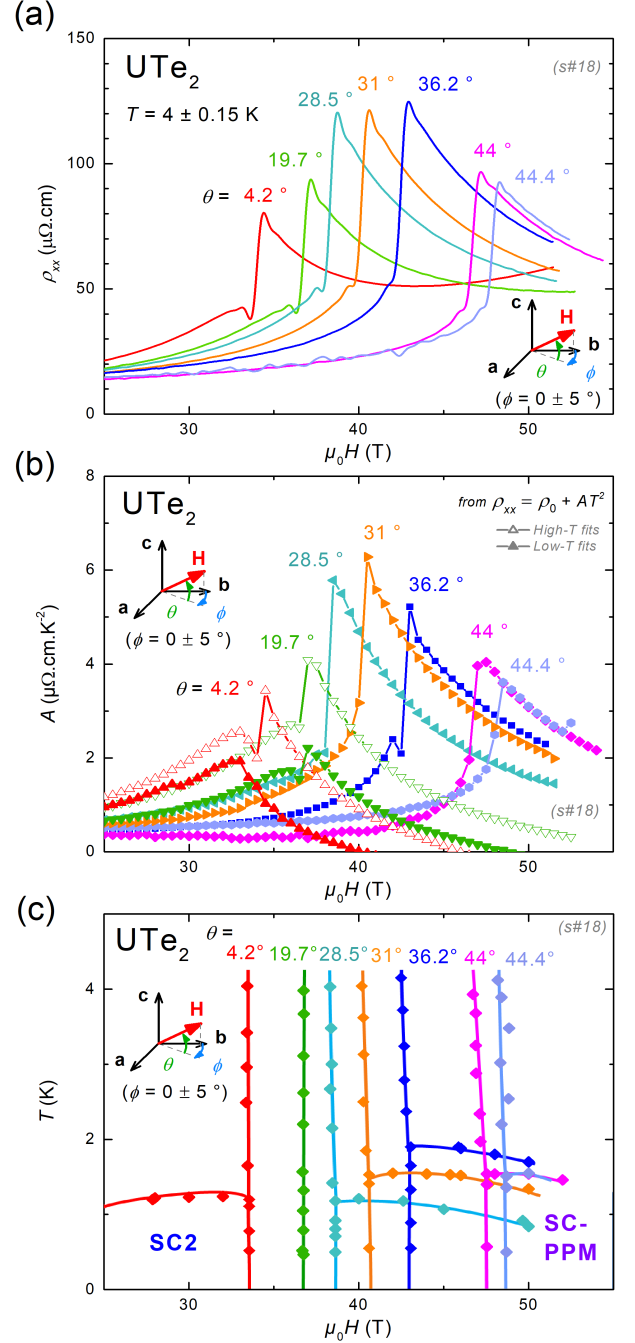


FIG. 2. Magnetic-field variations of (a) the electrical resistivity ρ_{xx} at $T = 4 \pm 0.15 \text{ K}$, (b) of the Fermi-liquid coefficient A , and (c) magnetic-field-temperature phase diagrams of UTe_2 under a magnetic field oriented with angles θ from 4.2 to 44.4°. Low- T and high- T fits were performed within temperature ranges $T_{sc}^{onset} < T \leq 4.2 \text{ K}$ and $2.1 \text{ K} \leq T \leq 4.2 \text{ K}$, respectively (see details in the Supplemental Material [41]).

tal Material [41]. Two kinds of fits were done here. At angles $\theta \leq 19.7^\circ$, low- T fits performed in the range $T_{sc} < T \leq 4 \text{ K}$ are affected by the cyclotron-motion effect, which leads to nonphysical negative values of A

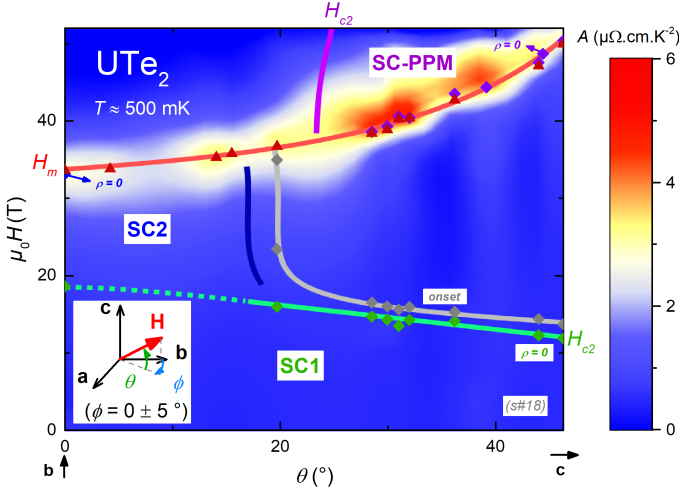


FIG. 3. Intensity map of the Fermi-liquid coefficient A as a function of H and $\theta = (\mathbf{b}, \mathbf{H})$ (for $\mathbf{H} \perp \mathbf{a}$). The intensity map combines data obtained on samples #18 and #19 (see details in the Supplemental Material [41]). The phase diagram shown on top of the intensity map was obtained from resistivity measurements on samples #18 and #19 at $T = 500$ mK.

at high fields. At these angles, high- T fits performed in the range $2.1 \text{ K} < T \leq 4 \text{ K}$ permit extracting a Fermi-liquid coefficient A , which is almost unaffected by the cyclotron-motion effect. At larger angles, the cyclotron-motion effect is absent and the two kinds of fits give similar results. For each magnetic-field direction, A reaches its maximal value A^{\max} at H_m , and A^{\max} is enhanced at $\theta \simeq 30^\circ$. For angles $\theta \geq 20^\circ$, the maximum of A at H_m is asymmetric, with a step-like increase for $H \lesssim H_m$ and a shoulder for $H \gtrsim H_m$. Fig. 2(c) shows a superposition of the magnetic-field-temperature phase diagrams obtained for the different field directions. For $\theta = 4.2^\circ$, SC2 is fully stabilized in fields $H < H_m$. For $\theta = 19.7^\circ$, the onset of SC2 is observed in fields $H < H_m$ but zero resistivity is not reached at low temperature. For $\theta > 19.7^\circ$, SC-PPM is stabilized in fields $H > H_m$. The critical temperature of SC-PPM reaches its maximum value $T_{SC-PPM}^{\max} \simeq 1.9 \text{ K}$ for $\theta = 36.2^\circ$.

An intensity map of A as a function of θ and H is presented in Fig. 3. It was obtained from high- T fits for $\theta < 20^\circ$ and low- T fits for $\theta \geq 20^\circ$, and it combines data from sample #18 (presented here) and sample #19 (see Supplemental Material [41]). The phase diagram of UTe_2 shown on top of the contour plot was obtained from data presented here on sample #18 at $T \simeq 500$ mK, the H_{c2} line of SC-PPM being taken from [11, 35]. The angle dependencies of the maximum in field A^{\max} of the Fermi-liquid coefficient (collected on samples #16, #18 and #19, see Supplemental Material [41]) and of the critical temperatures T_{SC2}^{\max} and T_{SC-PPM}^{\max} of SC2 and SC-PPM (collected on samples #16, #18 and #19, see Supplemental Material [41], and from [12, 35]) are presented

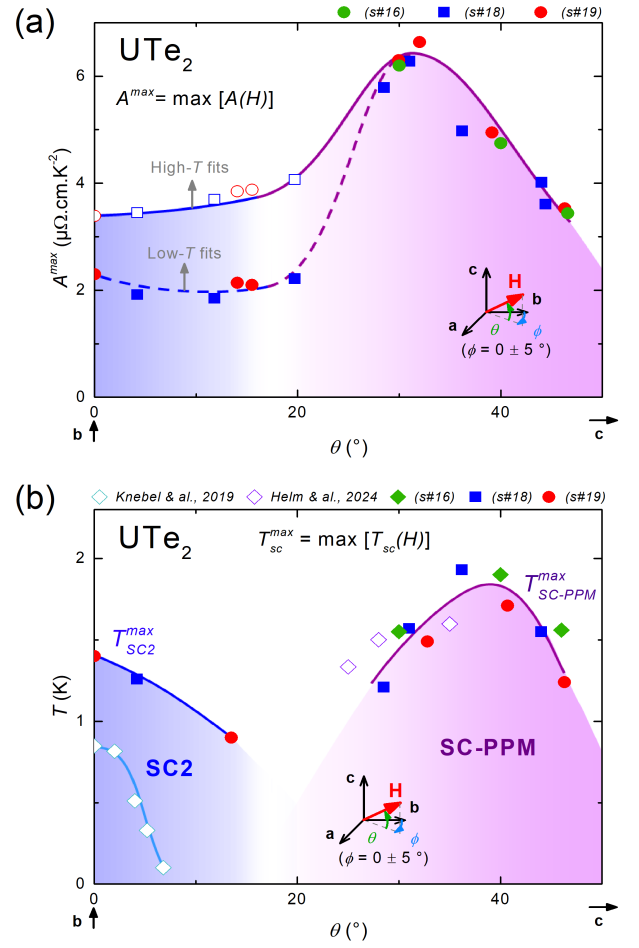


FIG. 4. (a) Angle- θ variation of $A^{\max} = \max[A(H)]$ extracted from the electrical resistivity of the three samples investigated here (#16, #18 and #19, see Supplemental Material [41]). The low- T and high- T fits were performed in the temperatures ranges $T_{sc} < T \leq 4 \text{ K}$ and $2.1 \text{ K} < T \leq 4 \text{ K}$, respectively. (b) Angle- θ variation the maximal critical temperatures T_{SC2}^{\max} and T_{SC-PPM}^{\max} of the superconducting phases SC2 and SC-PPM, respectively, extracted from studies on samples #16, #18 and #19 grown by the MSF method (#16, #18 and #19, see Supplemental Material [41]) and on samples grown by the chemical vapor transport (CVT) method (data from [12, 35]).

in Figs. 4(a,b), respectively. These plots show that A^{\max} is enhanced at angles $\theta \simeq 30 - 33^\circ$ while T_{SC-PPM}^{\max} is enhanced at angles $\theta \simeq 35 - 39^\circ$.

Signatures of enhanced electronic correlations have been found close to the metamagnetic field H_m . Similar variations of A [Fig. 2(a)] and ρ_{xx} at $T = 4 \text{ K}$ [Fig. 2(b)] have been observed, resulting from the contribution of magnetic fluctuations in the electrical resistivity. For $\mathbf{H} \parallel \mathbf{b}$, a Fermi-liquid behavior was also identified from earlier studies by electrical resistivity [31, 34], heat capacity [33, 37] and magnetization [32, 38], and enhanced magnetic fluctuations have been evidenced at H_m by NMR-relaxation-rate measurements [40]. The maximal

value A^{max} of the Fermi-liquid coefficient at H_m and the highest superconducting temperature T_{SC-PPM}^{max} of SC-PPM are found for a similar range of angles $30^\circ \lesssim \theta \lesssim 40^\circ$. This supports that the magnetic fluctuations which contribute to ρ_{xx} probably play a key role in the mechanism driving to SC-PPM. On the contrary, at low angles $\theta < 20^\circ$, A^{max} is almost constant while the highest superconducting temperature T_{SC2}^{max} of SC2 rapidly decreases with θ , and their variations in angle seem not to be simply correlated. The increase of A^{max} seems then too slow to overcome the superconducting-pair breaking induced by the magnetic field. To allow superconductivity at higher fields, larger values of A^{max} than those found for $\mathbf{H} \simeq \parallel \mathbf{b}$ are even needed to overcome the breaking effect, and larger values of A^{max} are indeed found here at angles $30^\circ \lesssim \theta \lesssim 40^\circ$. However, the situation is not so simple, since similar values of T_{SC-PPM}^{max} are found at angles $\theta = 31^\circ$ and 44.4° , but A^{max} is smaller for $\theta = 44.4^\circ$ than for $\theta = 31^\circ$.

Interestingly, large values of A extracted from ρ_{xx} are found, with an asymmetric shape, only above H_m , never below, at angles $30^\circ \lesssim \theta \lesssim 40^\circ$ [see Fig. 2(a) and Fig. S14 in the Supplemental Material [41]]. This may qualitatively explain the angular range for SC-PPM and the fact that it only occurs above H_m . In [34], an asymmetry in the variation of A through H_m was also observed for an angle $\theta = 41 \pm 2^\circ$ (initially estimated at $27 \pm 5^\circ$, see Supplemental Material [41]). A similar asymmetry was also observed in the Sommerfeld coefficient extracted, using thermodynamic relationships, from magnetization measurements performed with an angle $\theta \simeq 24^\circ$ [38]. On the contrary, a symmetric variation of A extracted from ρ_{xx} through H_m was observed in configurations where SC2 is stabilized for $H < H_m$, either for $\mathbf{H} \parallel \mathbf{b}$ and at small angles θ , or under pressure close to $p_c \simeq 1.5 - 1.7$ GPa combined with a magnetic field tilted with an angle $\theta \simeq 30^\circ$ [14, 46].

Beyond our work, further experiments on UTe_2 may help accessing new information about the magnetic fluctuations and their relation with the domains of stability of the magnetic-field-induced superconducting phases SC2 and SC-PPM. The magnetic fluctuations in UTe_2 , as in other U-based heavy-fermion systems, are a property of $5f$ electrons, which are part of the Fermi surface and contribute to the electrical resistivity. The effect of magnetic fluctuations to the electrical resistivity was modeled, assuming isotropic properties, for actinide metals and compounds in [47]. However, the electrical resistivity of UTe_2 strongly depends on the electrical-current direction [39, 48, 49] and one can suspect that its anisotropy may, at least partly, be related with the anisotropy of the magnetic fluctuations. A further investigation of UTe_2 by electrical resistivity with currents $\mathbf{I} \parallel \mathbf{b}, \mathbf{c}$ may permit accessing complementary information to that extracted here with a current $\mathbf{I} \parallel \mathbf{a}$. In parallel, a heat-capacity study would allow extracting the

field- and angle-variations of the Sommerfeld coefficient, which gives a direct information about the entropy associated with the magnetic fluctuations. Finally, NMR relaxation-rate studies of UTe_2 may also be performed to extract microscopic information about the magnetic-fluctuations modes implied in the stabilization of SC2 and SC-PPM. Such projects in rotating and intense magnetic fields request pushing up the experimental state of the art and constitute challenges to overcome for the next years.

ACKNOWLEDGEMENTS

We acknowledge financial support from the French National Research Agency collaborative research project FRESCO No. ANR-20-CE30-0020 and from the JSPS KAKENHI Grants Nos. JP19H00646, 19K03756, JP20H00130, 20H01864, JP20K20889, JP20KK0061, and 21H04987.

-
- [1] C. Pfleiderer, *Rev. Mod. Phys.* **81**, 1551 (2009).
 - [2] W. Knafo, arXiv:2107.13458 (2021).
 - [3] D. Aoki, K. Ishida, and J. Flouquet, *J. Phys. Soc. Jpn.* **88**, 022001 (2019).
 - [4] T. Hattori, Y. Ihara, Y. Nakai, K. Ishida, Y. Tada, S. Fujimoto, N. Kawakami, E. Osaki, K. Deguchi, N. Sato, *et al.*, *Phys. Rev. Lett.* **108**, 066403 (2012).
 - [5] B. Wu, G. Bastien, M. Taupin, C. Paulsen, L. Howald, D. Aoki, and J.-P. Brison, *Nat. Commun.* **8**, 14480 (2017).
 - [6] A. Miyake, D. Aoki, and J. Flouquet, *J. Phys. Soc. Jpn.* **77**, 094709 (2008).
 - [7] A. Miyake, D. Aoki, and J. Flouquet, *J. Phys. Soc. Jpn.* **78**, 063703 (2009).
 - [8] A. Gourgout, A. Pourret, G. Knebel, D. Aoki, G. Seyfarth, and J. Flouquet, *Phys. Rev. Lett.* **117**, 046401 (2016).
 - [9] Y. Tokunaga, D. Aoki, H. Mayaffre, S. Krämer, M.-H. Julien, C. Berthier, M. Horvatić, H. Sakai, S. Kambe, and S. Araki, *Phys. Rev. Lett.* **114**, 216401 (2015).
 - [10] Y. Tokunaga, D. Aoki, H. Mayaffre, S. Krämer, M.-H. Julien, C. Berthier, M. Horvatić, H. Sakai, T. Hattori, S. Kambe, and S. Araki, *Phys. Rev. B* **93**, 201112 (2016).
 - [11] S. Ran, I.-L. Liu, Y. S. Eo, D. J. Campbell, P. Neves, W. T. Fuhrman, S. R. Saha, C. Eckberg, H. Kim, J. Paglione, D. Graf, J. Singleton, and N. P. Butch, *Nat. Phys.* **15**, 1250 (2019).
 - [12] G. Knebel, W. Knafo, A. Pourret, Q. Niu, M. Vališka, D. Braithwaite, G. Lapertot, M. Nardone, A. Zitouni, S. Mishra, I. Sheikin, G. Seyfarth, J.-P. Brison, D. Aoki, and J. Flouquet, *J. Phys. Soc. Jpn.* **88**, 063707 (2019).
 - [13] D. Aoki, M. Kimata, Y. J. Sato, G. Knebel, F. Honda, A. Nakamura, D. Li, Y. Homma, Y. Shimizu, W. Knafo, D. Braithwaite, M. Vališka, A. Pourret, J.-P. Brison, and J. Flouquet, *J. Phys. Soc. Jpn.* **90**, 074705 (2021).
 - [14] M. Vališka, W. Knafo, G. Knebel, G. Lapertot, D. Aoki, and D. Braithwaite, *Phys. Rev. B* **104**, 214507 (2021).

- [15] Z. Wu, T. I. Weinberger, A. J. Hickey, D. V. Chichinadze, D. Shaffer, A. Cabala, H. Chen, M. Long, T. J. Brumm, W. Xie, Y. Ling, Z. Zhu, Y. Skourski, D. E. Graf, V. Sechovský, M. Vališka, G. G. Lonzarich, F. M. Grosche, and A. G. Eaton, *Phys. Rev. X* **15**, 021019 (2025).
- [16] S. K. Lewin, P. Czajka, C. E. Frank, G. S. Salas, H. Yoon, Y. S. Eo, J. Paglione, A. H. Nevidomskyy, J. Singleton, and N. P. Butch, arXiv:2402.18564 (2024).
- [17] C. E. Frank, S. K. Lewin, G. Saucedo Salas, P. Czajka, I. M. Hayes, H. Yoon, T. Metz, J. Paglione, J. Singleton, and N. P. Butch, *Nat. Commun.* **15**, 3378 (2024).
- [18] S. Ran, C. Eckberg, Q.-P. Ding, Y. Furukawa, T. Metz, S. R. Saha, I.-L. Liu, M. Zic, H. Kim, J. Paglione, and N. P. Butch, *Science* **365**, 684 (2019).
- [19] D. Aoki, A. Nakamura, F. Honda, D. Li, Y. Homma, Y. Shimizu, Y. J. Sato, G. Knebel, J.-P. Brison, A. Pourret, D. Braithwaite, G. Lapertot, Q. Niu, M. Vališka, H. Harima, and J. Flouquet, *J. Phys. Soc. Jpn.* **88**, 043702 (2019).
- [20] K. Kinjo, H. Fujibayashi, H. Matsumura, F. Hori, S. Kitagawa, K. Ishida, Y. Tokunaga, H. Sakai, S. Kambe, A. Nakamura, *et al.*, *Sci. Adv.* **9**, eadg2736 (2023).
- [21] F. Theuss, A. Shragai, G. Grissonnanche, L. Peralta, G. d. I. F. Simarro, I. M. Hayes, S. R. Saha, Y. S. Eo, A. Suarez, A. C. Salinas, G. Pokharel, S. D. Wilson, N. P. Butch, J. Paglione, and B. J. Ramshaw, *Nat. Phys.* **1**, 1 (2024).
- [22] C. Duan, K. Sasmal, M. B. Maple, A. Podlesnyak, J.-X. Zhu, Q. Si, and P. Dai, *Phys. Rev. Lett.* **125**, 237003 (2020).
- [23] W. Knafo, G. Knebel, P. Steffens, K. Kaneko, A. Rosuel, J.-P. Brison, J. Flouquet, D. Aoki, G. Lapertot, and S. Raymond, *Phys. Rev. B* **104**, L100409 (2021).
- [24] N. P. Butch, S. Ran, S. R. Saha, P. M. Neves, M. P. Zic, J. Paglione, S. Gladchenko, Q. Ye, and J. A. Rodriguez-Rivera, *npj Quantum Mater.* **7**, 39 (2022).
- [25] C. Duan, R. Baumbach, A. Podlesnyak, Y. Deng, C. Moir, A. J. Breindel, M. B. Maple, E. Nica, Q. Si, and P. Dai, *Nature* **600**, 636 (2021).
- [26] S. Raymond, W. Knafo, G. Knebel, K. Kaneko, J.-P. Brison, J. Flouquet, D. Aoki, and G. Lapertot, *J. Phys. Soc. Jpn.* **90**, 113706 (2021).
- [27] W. Knafo, T. Thebault, P. Manuel, D. Khalyavin, F. Orlandi, E. Ressouche, K. Beauvois, G. Lapertot, K. Kaneko, D. Aoki, D. Braithwaite, G. Knebel, and S. Raymond, arXiv:2311.05455 (2023).
- [28] Y. Tokunaga, H. Sakai, S. Kambe, T. Hattori, N. Higa, G. Nakamine, S. Kitagawa, K. Ishida, A. Nakamura, Y. Shimizu, Y. Homma, D. Li, F. Honda, and D. Aoki, *J. Phys. Soc. Jpn.* **88**, 073701 (2019).
- [29] H. Fujibayashi, K. Kinjo, G. Nakamine, S. Kitagawa, K. Ishida, Y. Tokunaga, H. Sakai, S. Kambe, A. Nakamura, Y. Shimizu, Y. Homma, D. Li, F. Honda, and D. Aoki, *J. Phys. Soc. Jpn.* **92** (2023), 10.7566/JPSJ.92.053702.
- [30] H. Matsumura, S. Kitagawa, S. Ogata, R. Matsubayashi, H. Fujibayashi, K. Kinjo, K. Ishida, Y. Tokunaga, H. Sakai, S. Kambe, A. Nakamura, Y. Shimizu, Y. Homma, D. Li, F. Honda, A. Miyake, and D. Aoki, *Phys. Rev. B* **111**, 094507 (2025).
- [31] W. Knafo, M. Vališka, D. Braithwaite, G. Lapertot, G. Knebel, A. Pourret, J.-P. Brison, J. Flouquet, and D. Aoki, *J. Phys. Soc. Jpn.* **88**, 063705 (2019).
- [32] A. Miyake, Y. Shimizu, Y. J. Sato, D. Li, A. Nakamura, Y. Homma, F. Honda, J. Flouquet, M. Tokunaga, and D. Aoki, *J. Phys. Soc. Jpn.* **88**, 063706 (2019).
- [33] A. Rosuel, C. Marcenat, G. Knebel, T. Klein, A. Pourret, N. Marquardt, Q. Niu, S. Rousseau, A. Demuer, G. Seyfarth, G. Lapertot, D. Aoki, D. Braithwaite, J. Flouquet, and J.-P. Brison, *Phys. Rev. X* **13**, 011022 (2023).
- [34] W. Knafo, M. Nardone, M. Vališka, A. Zitouni, G. Lapertot, D. Aoki, G. Knebel, and D. Braithwaite, *Commun. Phys.* **4**, 40 (2021).
- [35] T. Helm, M. Kimata, K. Sudo, A. Miyata, J. Stirnat, T. Förster, J. Hornung, M. König, I. Sheikin, A. Pourret, G. Lapertot, D. Aoki, G. Knebel, J. Wosnitza, and J.-P. Brison, *Nat. Commun.* **15**, 37 (2024).
- [36] S. K. Lewin, J. J. Yu, C. E. Frank, D. Graf, P. Chen, S. Ran, Y. S. Eo, J. Paglione, S. Raghu, and N. P. Butch, arXiv:2410.05137 (2024).
- [37] S. Imajo, Y. Kohama, A. Miyake, C. Dong, M. Tokunaga, J. Flouquet, K. Kindo, and D. Aoki, *J. Phys. Soc. Jpn.* **88**, 083705 (2019).
- [38] A. Miyake, Y. Shimizu, Y. J. Sato, D. Li, A. Nakamura, Y. Homma, F. Honda, J. Flouquet, M. Tokunaga, and D. Aoki, *J. Phys. Soc. Jpn.* **90**, 103702 (2021).
- [39] T. Thebault, M. Vališka, G. Lapertot, A. Pourret, D. Aoki, G. Knebel, D. Braithwaite, and W. Knafo, *Phys. Rev. B* **106**, 144406 (2022).
- [40] Y. Tokunaga, H. Sakai, S. Kambe, P. Opletal, Y. Tokiwa, Y. Haga, S. Kitagawa, K. Ishida, D. Aoki, G. Knebel, G. Lapertot, S. Krämer, and M. Horvatić, *Phys. Rev. Lett.* **131**, 226503 (2023).
- [41] See Supplemental Material for details.
- [42] H. Sakai, P. Opletal, Y. Tokiwa, E. Yamamoto, Y. Tokunaga, S. Kambe, and Y. Haga, *Phys. Rev. Mater.* **6**, 073401 (2022).
- [43] J. Béard, J. Billette, N. Ferreira, P. Frings, J.-M. Lagarrigue, F. Lecouturier, and J.-P. Nicolin, *IEEE Trans. Appl. Supercond.* **28**, 1 (2018).
- [44] D. Aoki, H. Sakai, P. Opletal, Y. Tokiwa, J. Ishizuka, Y. Yanase, H. Harima, A. Nakamura, D. Li, Y. Homma, Y. Shimizu, G. Knebel, J. Flouquet, and Y. Haga, *J. Phys. Soc. Jpn.* **91**, 083704 (2022).
- [45] Y. Onuki, *Physics of Heavy Fermions: Heavy Fermions and Strongly Correlated Electrons Systems* (World Scientific, 2018).
- [46] T. Thebault, D. Braithwaite, G. Lapertot, D. Aoki, G. Knebel, and W. Knafo, *Phys. Rev. B* **109**, 214420 (2024).
- [47] R. Jullien, M. Beal-Monod, and B. Coqblin, *Phys. Rev. B* **9**, 1441 (1974).
- [48] Y. S. Eo, S. Liu, S. R. Saha, H. Kim, S. Ran, J. A. Horn, H. Hodovanets, J. Collini, T. Metz, W. T. Fuhrman, A. H. Nevidomskyy, J. D. Denlinger, N. P. Butch, M. S. Fuhrer, L. A. Wray, and J. Paglione, *Phys. Rev. B* **106**, L060505 (2022).
- [49] G. Knebel, A. Pourret, S. Rousseau, N. Marquardt, D. Braithwaite, F. Honda, D. Aoki, G. Lapertot, W. Knafo, G. Seyfarth, J.-P. Brison, and J. Flouquet, *Phys. Rev. B* **109**, 155103 (2024).

Supplemental Material:

Field-induced electronic correlations and superconductivity in UTe_2 beyond 40 T

Experimental details are given and supplemental figures are shown for the different investigated samples. Details about raw data and their analysis to construct magnetic-field-temperature phase diagrams and to extract the Fermi-liquid coefficient A are given. We also show that a flux-flow resistive signal persists in the superconducting phase SC1 for $\mathbf{H} \approx \parallel \mathbf{b}$ in these samples grown by the molten-salt-flux technique.

Experimental details

Four UTe_2 single crystals (samples #16, #18, #19 and #20) have been investigated here by electrical resistivity. In complement to the paper, which presents data from samples #18 and #20, this Supplemental Material shows data collected from the three samples #16, #18 and #19, supporting the reproducibility of our results. The four samples have been grown by the molten-salt-flux (MSF) method [S1]. Their electrical resistivity was measured with a current $\mathbf{I} \parallel \mathbf{a}$ under magnetic fields up to 55 T applied in the (\mathbf{b}, \mathbf{c}) plane for samples #16, #18 and #19 and under magnetic fields $\mu_0 \mathbf{H} \parallel \mathbf{b}$ up to 95 T for sample #20. A single-axis rotator was used to change the field direction defined by the angle $\theta = (\mathbf{H}, \mathbf{b})$ (with $\mathbf{H} \perp \mathbf{a}$). The samples #18, #19 and #20 were selected with a clean face perpendicular to \mathbf{c} , with dimensions of approximately 1-2 mm along \mathbf{a} , 0.3-0.5 mm along \mathbf{b} , and 0.1-0.2 mm along \mathbf{c} . The sample #16 was selected with a clean face perpendicular to the plane of Miller indices (011), with similar dimensions than samples #18 and #19. The orientation of the crystals was ensured by Laue diffraction. Four electrical contacts with 15- μm gold wires were spot-welded on sample surfaces. The electrical resistivity was measured with an excitation current of 10 mA and a frequency $f \approx 40$ kHz. Pulsed magnetic-field experiments were performed using a long-duration 60-T single-coil magnet (pulses rise of 50 ms and fall of 280 ms) and a > 90 -T triple-coil magnet (inner coil permitting to reach the maximum magnetic field: pulses rise of 6 ms and fall of 13 ms) at the Laboratoire National des Champs Magnétiques Intenses (LNCMI) in Toulouse (see Figure S1). Samples #16, #18 and #19 were investigated at temperatures from 470 mK to 10 K delivered by an ^3He insert combined with a ^4He cryostat, and sample #20 was investigated at temperatures from 1.4 K to 36.5 K using a ^4He cryostat.

Electrical resistivity and phase diagrams

Figures S2 and S3 present the field variation of the electrical resistivity ρ_{xx} of UTe_2 samples #18 and #19, respectively, at temperatures T from 500 mK to 10 K, in magnetic fields up to 55 T with angles $\theta = (\mathbf{H}, \mathbf{b})$ varying from 0° ($\mathbf{H} \parallel \mathbf{b}$) to 46° . These data were collected during the fall of the pulsed magnetic fields. The magnetic-field temperature phase diagrams obtained from these resistivity data are presented in Figures S4 (sample #18) and S5 (sample #19).

Figure S6 shows the angle-magnetic-field phase diagram of UTe_2 obtained at low temperatures, combining data collected here on samples #18 and #19 and data published in the literature [S2–S9]. Figure S7(a,b) show intensity maps of the electrical resistivity of UTe_2 sample #18 measured at $T = 500$ mK and $T = 4$ K, respectively, as a function of θ and H . The phase diagram shown on top of the intensity maps was obtained from resistivity measurements on samples #18 and #19 at $T = 500$ mK. Figure S7(a) illustrates that the domains of stability of SC2 and SC-PPM correspond to zero-resistivity (or nearly-zero resistivity, see Section S4) states. Figure S7(b) shows that an enhancement of $\rho_{xx}(T = 4 \text{ K})$ is observed in the vicinity of SC-PPM, for $H \gtrsim H_m$ and angles $30^\circ \lesssim \theta \lesssim 40^\circ$. This enhancement of the electronic correlations visible at $T = 4$ K is attributed to a magnetic-fluctuation mode, which also drives the enhancement of the Fermi-liquid coefficient A in the same field and angle regime (see Figure 3 of the paper). This magnetic-fluctuations mode is suspected to be involved in the mechanism driving the superconducting phase SC-PPM.

Fermi-liquid coefficient A

Figures S8 and S9 present details about the low- T Fermi-liquid fits to the data by $\rho_{xx} = \rho_0 + AT^2$ used to extract the coefficient A , for samples #18 and #19, respectively. The T^2 variation of ρ_{xx} in magnetic fields up to 50 T and the fits to the data are presented for all directions of magnetic field investigated, with angles θ varying from 0° ($\mathbf{H} \parallel \mathbf{b}$) to 46° .

Figure S10(a) presents a comparison between low- T and high- T Fermi-liquid fits to the data collected on sample #18 in magnetic fields of 0.5, 36 and 50 T applied with the angle $\theta = 4.2^\circ$. The low- T and high- T fits have been performed in temperature ranges $T_{sc} < T \leq 4.2$ K and $2.1 \text{ K} \leq T \leq 4.2$ K, respectively. For field directions close to \mathbf{b} , i.e., at low angles θ , an increase of ρ_{xx} at low temperature and high field is attributed to a carriers cyclotron-motion effect, which is induced in the highest-quality samples. The cyclotron-motion effect leads to reduced fitted values of A , which take here non-physical negative values at the highest fields. Figure S10(b) presents the field variation of A extracted from electrical-resistivity ρ_{xx} data collected on samples #1, #2 and #3 in a magnetic field $\mathbf{H} \parallel \mathbf{b}$, which have been grown by the chemical vapor transport (CVT) method (data from [S10]). In comparison with the MSF samples, the CVT samples have a lower quality, as indicated by a lower residual-resistivity ratio [S11] and a smaller

cyclotron-motion effect. The CVT samples #1, #2 and #3 do not show a cyclotron-motion contribution to ρ_{xx} at high fields and low temperatures, and they can be considered as a reference for a coefficient A not affected by the cyclotron-motion effect. Figure S10(b) shows that the field variations of A extracted from high- T fits on sample #18 and extracted from low- T fits on samples #1, #2 and #3 are very similar, supporting that the high- T fits permit extracting a coefficient A , which is weakly affected by the cyclotron-motion effect on our MSF samples.

Figures S11 and S12 show a comparison of the magnetic-field variations of A extracted from low- T and high- T fits to ρ_{xx} on samples #18 and #19, respectively, for each of the angles θ investigated here. Similar results are obtained for samples #18 and #19. For angles $\theta > 20^\circ$, no cyclotron motion is detected and the two types of fits give similar results.

Figure S13 shows the magnetic-field variation of the residual resistivity ρ_0 extracted for sample #18 from low- T and high- T fits to ρ_{xx} for angles $\theta < 20^\circ$ and from low- T fits to ρ_{xx} for angles $\theta > 20^\circ$. A jump in the residual resistivity occurs at the metamagnetic transition as previously reported in [S4, S10, S12]. For $\theta < 20^\circ$, ρ_0 increases in high fields due to the cyclotron-motion effect, whose signatures are not observed for $\theta > 20^\circ$.

Figure S14 shows the variation of A extracted from Fermi-liquid fits to the electrical resistivity of UTe₂ sample #18, for $4.2^\circ \leq \theta \leq 44.4^\circ$ (from high- T fits for $\theta < 20^\circ$ and low- T fits for $\theta > 20^\circ$) as a function of H/H_m . It emphasizes that, while A has a rather symmetric variation through H_m at low angles $\theta < 20^\circ$, its variation becomes asymmetric through H_m at angles $\theta < 20^\circ$, with a shoulder indicative of enhanced correlations developing for $\theta > 20^\circ$.

Figure S15 compares the magnetic-field variations of A extracted for different angles θ on the three samples (#16, #18, and #19) grown by the MSF technique investigated here and on other samples (#1, #2, #3, #5, #6, and #7) grown by the CVT technique and investigated in [S4, S10, S13]. Samples #18 and #19 have been studied in angles $0 \leq \theta \leq 46^\circ$ and sample #16 has been studied in angles $30 \leq \theta \leq 46^\circ$. Samples #1, #2, #3 and #5 have been studied in a magnetic field $\mathbf{H} \parallel \mathbf{b}$ with $\theta = 0^\circ$. Samples #5, #6, and #7 have also been studied in a magnetic field tilted by an angle initially estimated by $\theta = 27 \pm 5^\circ$ using a sample holder with a fixed tilted direction. However, different values of the metamagnetic field indicate different angles, which were re-estimated here to $\theta = 24.8^\circ$ for sample #5, $\theta = 40^\circ$ for sample #6, and $\theta = 40.7$ and 41° for sample #7, assuming no tilt of the magnetic field towards the direction \mathbf{a} , from the now-well-characterized angle- θ dependence of H_m (see Figure S6 and [S3, S5–S9]). The data compiled in Figure S15 show similar variations of A as a function of H and θ and demonstrate the reproducibility of the results presented in our paper.

Flux-flow resistivity

Figures S16(a-b) present a zoom on ρ_{xx} measured on samples #18 and #19, respectively, at temperatures $T < 1.4$ K and magnetic fields $\mu_0 \mathbf{H} \approx \parallel \mathbf{b}$ up to 25 T. At the lowest temperatures, we find that, instead of a perfectly zero resistivity, a small contribution to the electrical resistivity is measured in the superconducting state. It results from the combination of two effects. The first one is a capacitive effect due to non-perfect electrical contacts on the sample, inducing a non-intrinsic contribution $\Delta\rho_{cap} \simeq 0.5 \mu\Omega\text{cm}$ to the electrical resistivity, measured here at a high frequency of $\simeq 40$ kHz. As shown in Figures S16(c-d), this capacitive effect is smaller at smaller frequencies $\simeq 15 - 19$ kHz. The second effect results from a flux-flow contribution to the high-field electrical resistivity, which is observed here in the superconducting phase SC1, but not in the superconducting phase SC2. Two kinks observed in the electrical resistivity at $T = 500$ mK at the magnetic fields $\mu_0 H_{k1}$ and $\mu_0 H_{k2}$, which reach 8.2 T and 17.6 T in sample #18, and 7.5 T and 18.7 T in sample #19, respectively, are attributed to the flux-flow contribution to ρ_{xx} . Figures S16(e-f) presents the magnetic-field-temperature phase diagrams obtained on samples #18 and #19, respectively, in magnetic fields $\mu_0 \mathbf{H} \approx \parallel \mathbf{b}$. The temperature dependence of H_{k2} coincides with that of the critical field H_{c2} delimiting the superconducting phase SC1, which was determined by heat-capacity measurements in [S14]. This indicates that SC1 is associated with a larger flux-flow resistivity than SC2. Flux-flow contributions to the electrical resistivity ρ_{xx} of UTe₂ under a magnetic field $\mathbf{H} \approx \parallel \mathbf{b}$ have also been observed in [S15, S16].

-
- [S1] H. Sakai, P. Opletal, Y. Tokiwa, E. Yamamoto, Y. Tokunaga, S. Kambe, and Y. Haga, *Phys. Rev. Mater.* **6**, 073401 (2022).
[S2] G. Knebel, W. Knafo, A. Pourret, Q. Niu, M. Vališka, D. Braithwaite, G. Lapertot, M. Nardone, A. Zitouni, S. Mishra, I. Sheikin, G. Seyfarth, J.-P. Brison, D. Aoki, and J. Flouquet, *J. Phys. Soc. Jpn.* **88**, 063707 (2019).
[S3] S. Ran, I.-L. Liu, Y. S. Eo, D. J. Campbell, P. Neves, W. T. Fuhrman, S. R. Saha, C. Eckberg, H. Kim, J. Paglione, D. Graf, J. Singleton, and N. P. Butch, *Nat. Phys.* **15**, 1250 (2019).

- [S4] W. Knafo, M. Nardone, M. Vališka, A. Zitouni, G. Lapertot, D. Aoki, G. Knebel, and D. Braithwaite, [Commun. Phys.](#) **4**, 40 (2021).
- [S5] R. Schöнемann, P. F. Rosa, S. M. Thomas, Y. Lai, D. N. Nguyen, J. Singleton, E. L. Brosha, R. D. McDonald, V. Zapf, B. Maiorov, *et al.*, arXiv:2206.06508 (2022).
- [S6] C. E. Frank, S. K. Lewin, G. Saucedo Salas, P. Czajka, I. M. Hayes, H. Yoon, T. Metz, J. Paglione, J. Singleton, and N. P. Butch, [Nat. Commun.](#) **15**, 3378 (2024).
- [S7] Z. Wu, T. Weinberger, J. Chen, A. Cabala, D. Chichinadze, D. Shaffer, J. Pospíšil, J. Prokleška, T. Haidamak, G. Bastien, *et al.*, [Proc. Natl. Acad. Sci. U.S. A.](#) **121**, e2403067121 (2024).
- [S8] T. Helm, M. Kimata, K. Sudo, A. Miyata, J. Stirnat, T. Förster, J. Hornung, M. König, I. Sheikin, A. Pourret, G. Lapertot, D. Aoki, G. Knebel, J. Wosnitza, and J.-P. Brison, [Nat. Commun.](#) **15**, 37 (2024).
- [S9] S. K. Lewin, P. Czajka, C. E. Frank, G. S. Salas, H. Yoon, Y. S. Eo, J. Paglione, A. H. Nevidomskyy, J. Singleton, and N. P. Butch, arXiv:2402.18564 (2024).
- [S10] W. Knafo, M. Vališka, D. Braithwaite, G. Lapertot, G. Knebel, A. Pourret, J.-P. Brison, J. Flouquet, and D. Aoki, [J. Phys. Soc. Jpn.](#) **88**, 063705 (2019).
- [S11] D. Aoki, I. Sheikin, N. Marquardt, G. Lapertot, J. Flouquet, and G. Knebel, [J. Phys. Soc. Jpn.](#) **93**, 123702 (2024).
- [S12] G. Knebel, A. Pourret, S. Rousseau, N. Marquardt, D. Braithwaite, F. Honda, D. Aoki, G. Lapertot, W. Knafo, G. Seyfarth, J.-P. Brison, and J. Flouquet, [Phys. Rev. B](#) **109**, 155103 (2024).
- [S13] W. Knafo, “unpublished.”
- [S14] A. Rosuel, C. Marcenat, G. Knebel, T. Klein, A. Pourret, N. Marquardt, Q. Niu, S. Rousseau, A. Demuer, G. Seyfarth, G. Lapertot, D. Aoki, D. Braithwaite, J. Flouquet, and J.-P. Brison, [Phys. Rev. X](#) **13**, 011022 (2023).
- [S15] H. Sakai, Y. Tokiwa, P. Opletal, M. Kimata, S. Awaji, T. Sasaki, D. Aoki, S. Kambe, Y. Tokunaga, and Y. Haga, [Phys. Rev. Lett.](#) **130**, 196002 (2023).
- [S16] Y. Tokiwa, H. Sakai, S. Kambe, P. Opletal, E. Yamamoto, M. Kimata, S. Awaji, T. Sasaki, Y. Yanase, Y. Haga, *et al.*, [Phys. Rev. B](#) **108**, 144502 (2023).

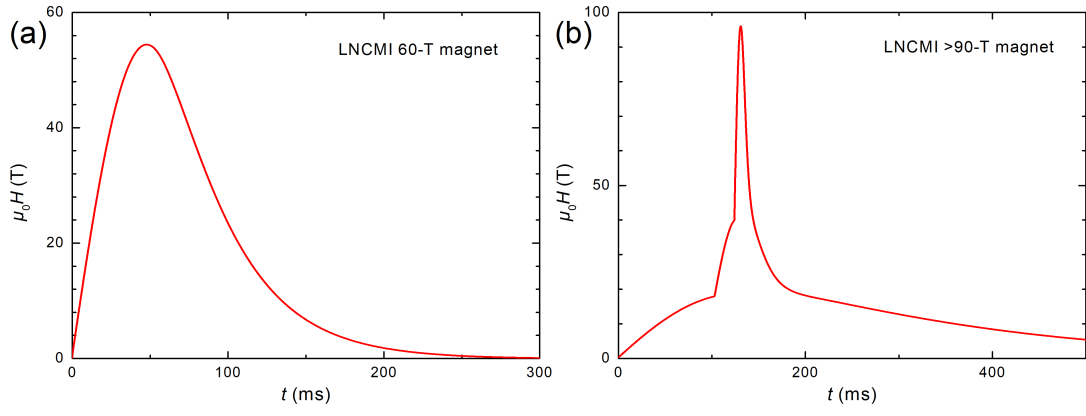


FIG. S1. Time profiles of magnetic fields generated by the (a) 60-T single-coil magnet and (b) > 90-T triple-coil magnet used in this study.

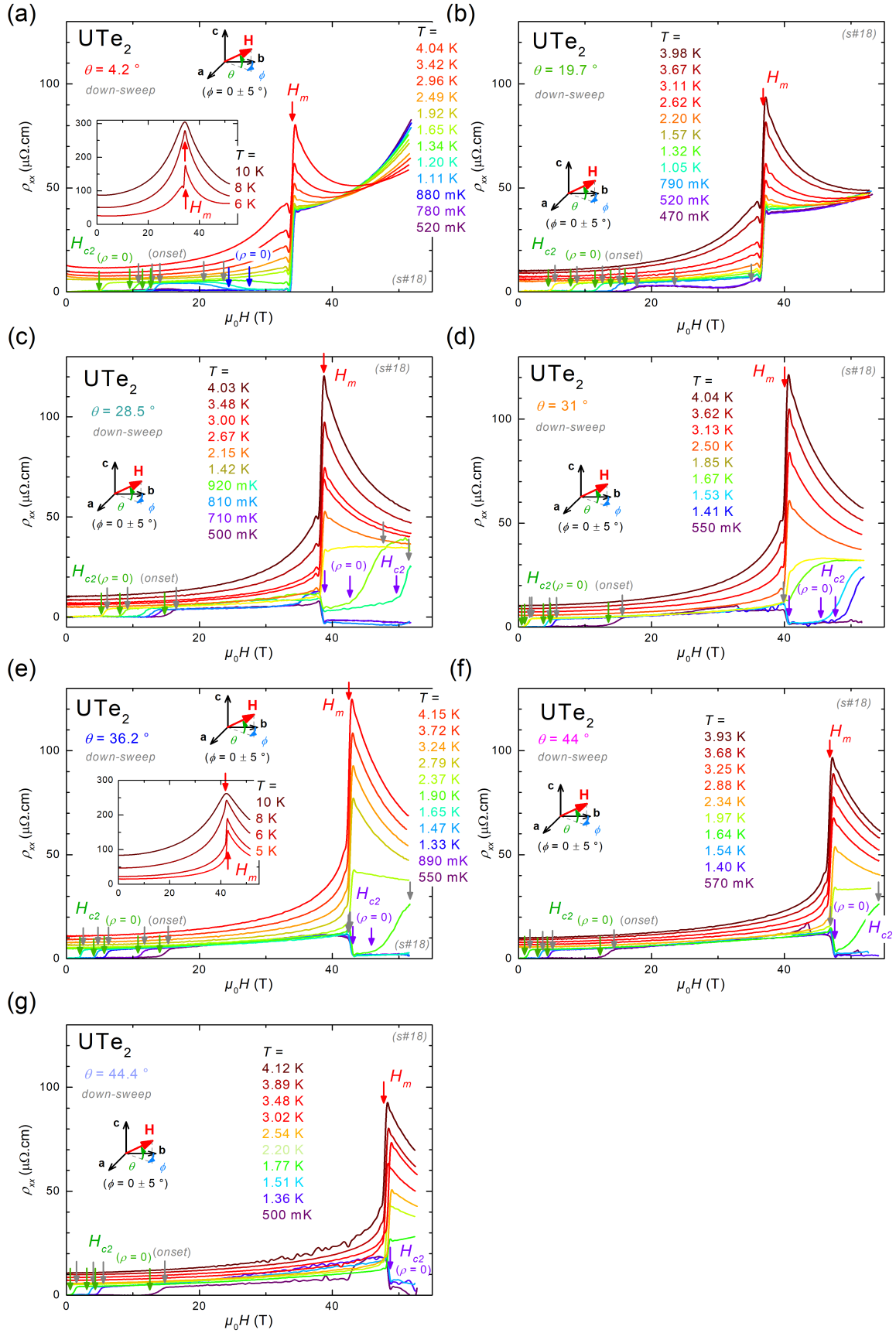


FIG. S2. Electrical resistivity ρ_{xx} of UTe_2 sample #18 versus magnetic field up to 55 T, at temperatures T from 500 mK to 10 K, for field directions with the angles $\theta =$ (a) 4.2° , (b) 19.7° , (c) 28.5° , (d) 31° , (e) 36.2° , (f) 44° , and (g) 44.4° . The data have been obtained during the fall of the pulsed magnetic field.

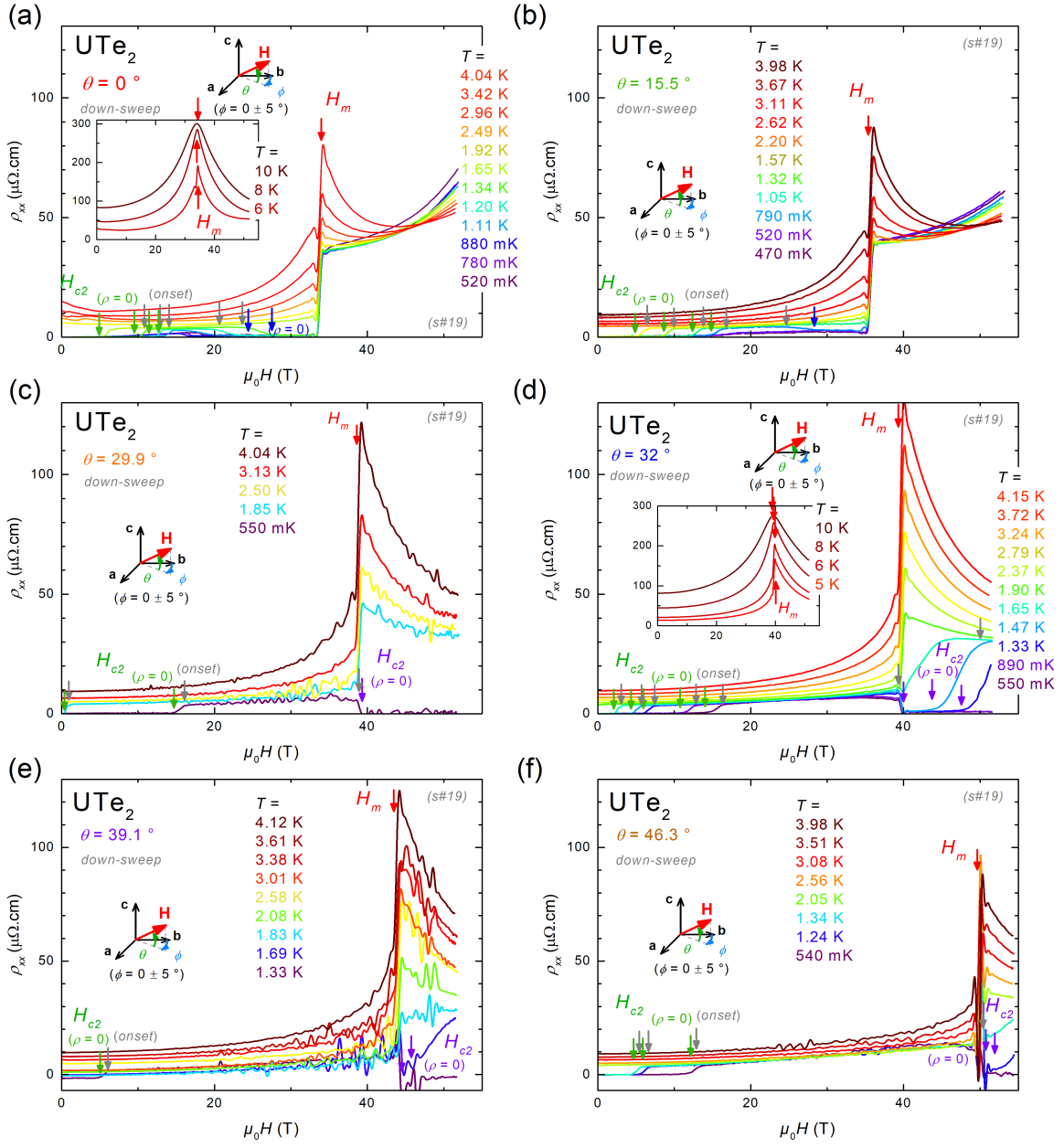


FIG. S3. Electrical resistivity ρ_{xx} of UTe₂ sample #19 versus magnetic field up to 55 T, at temperatures T from 500 mK to 10 K, for field directions with the angles $\theta =$ (a) 0° , (b) 15.5° , (c) 29.9° , (d) 32° , (e) 39.1° , and (f) 46.3° . The data have been obtained during the fall of the pulsed magnetic field.

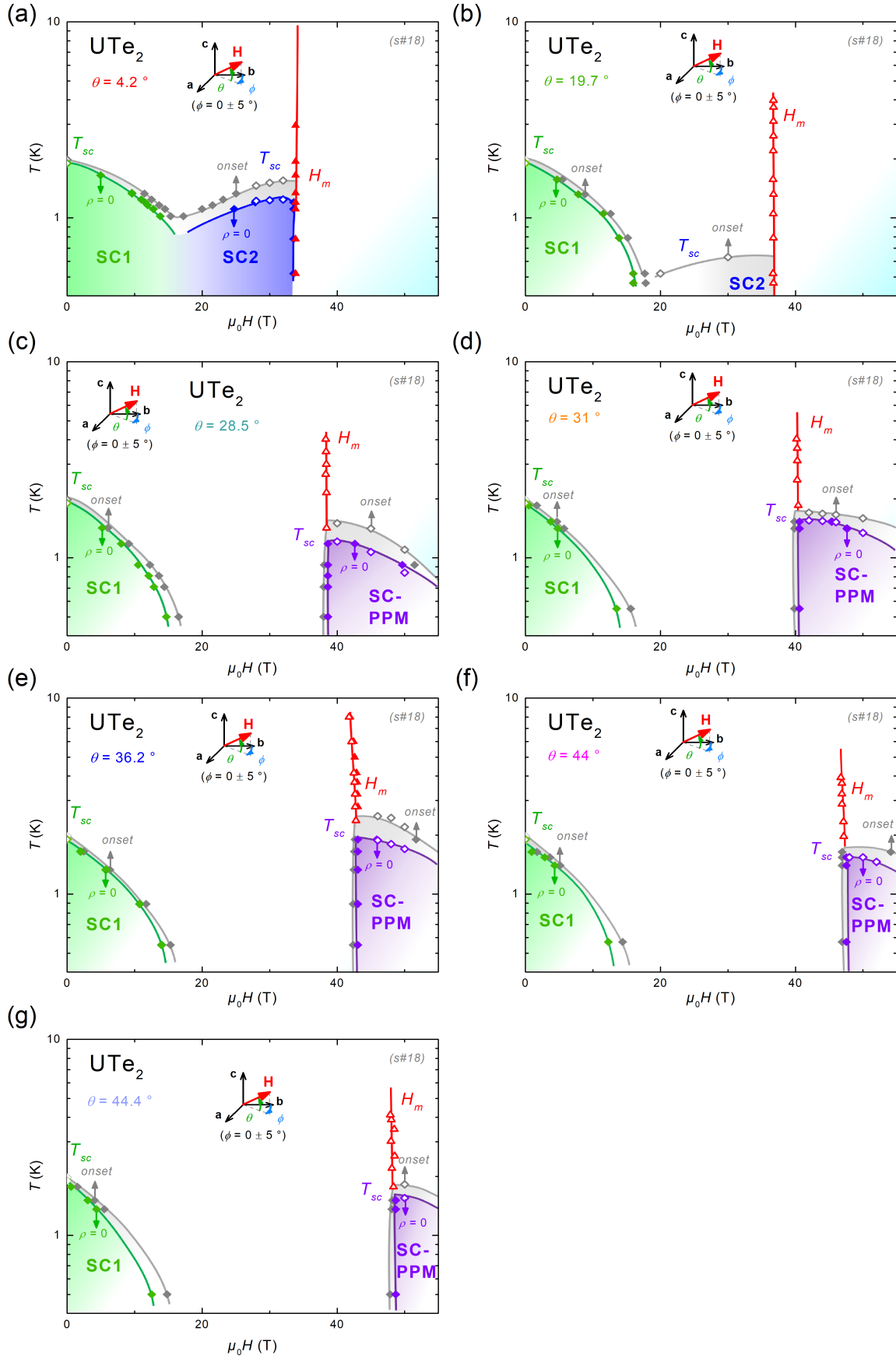


FIG. S4. Magnetic-field-temperature phase diagrams obtained from our resistivity measurements on sample #18 for $\theta =$ (a) 4.2° , (b) 19.7° , (c) 28.5° , (d) 31° , (e) 36.2° , (f) 44° , and (g) 44.4° .

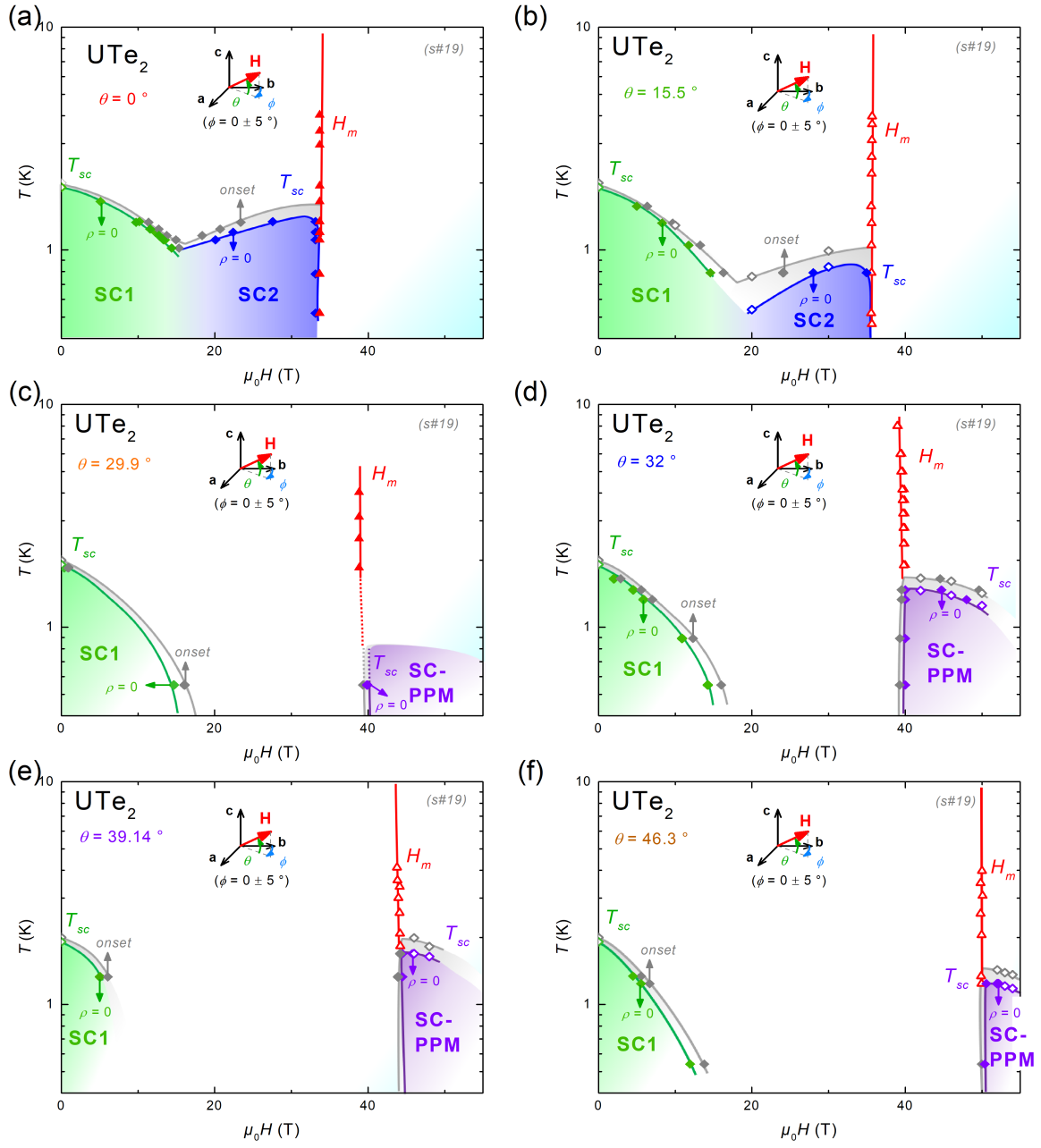


FIG. S5. Magnetic-field-temperature phase diagrams obtained from our resistivity measurements on sample #19 for $\theta =$ (a) 0° , (b) 15.5° , (c) 29.9° , (d) 32° , (e) 39.1° , and (f) 46.3° .

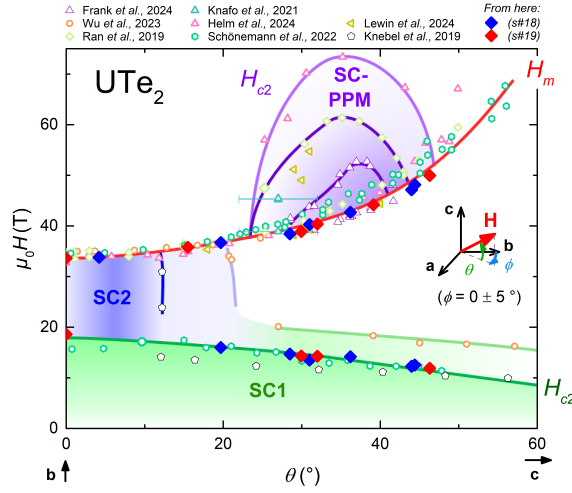


FIG. S6. Angle-magnetic-field phase diagram of UTe_2 in the limit of $T \rightarrow 0$, from a compilation of data collected here on samples #18 and #19 and from [S2–S9]

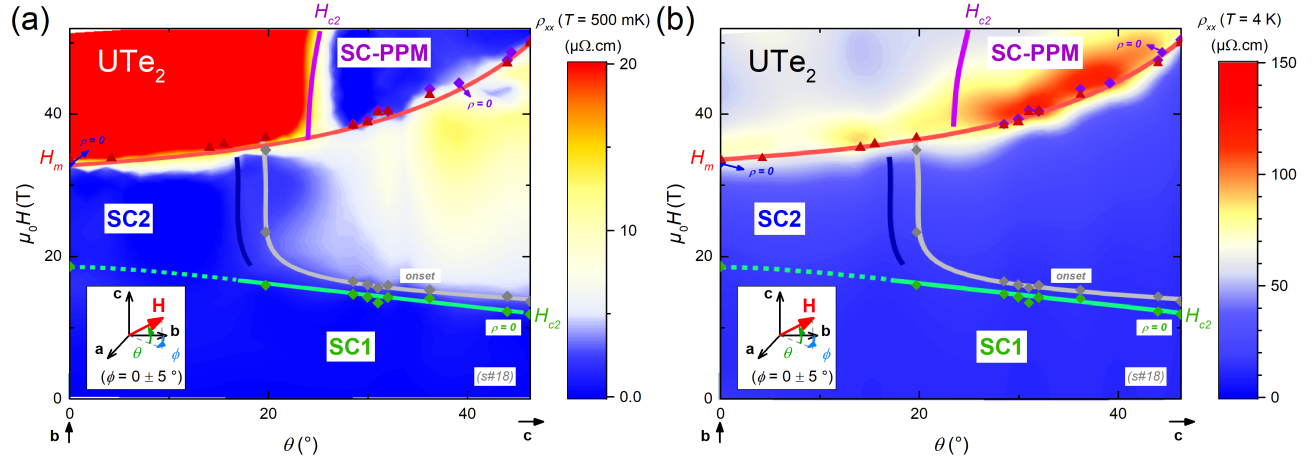


FIG. S7. Intensity maps of the electrical resistivity of UTe_2 sample #18 measured at (a) $T = 500$ mK and (b) $T = 4$ K, as a function of $\theta = (\mathbf{b}, \mathbf{H})$ and H (for $\mathbf{H} \perp \mathbf{a}$). The phase diagram shown on top of the intensity maps was obtained from resistivity measurements on samples #18 and #19 at $T = 500$ mK.

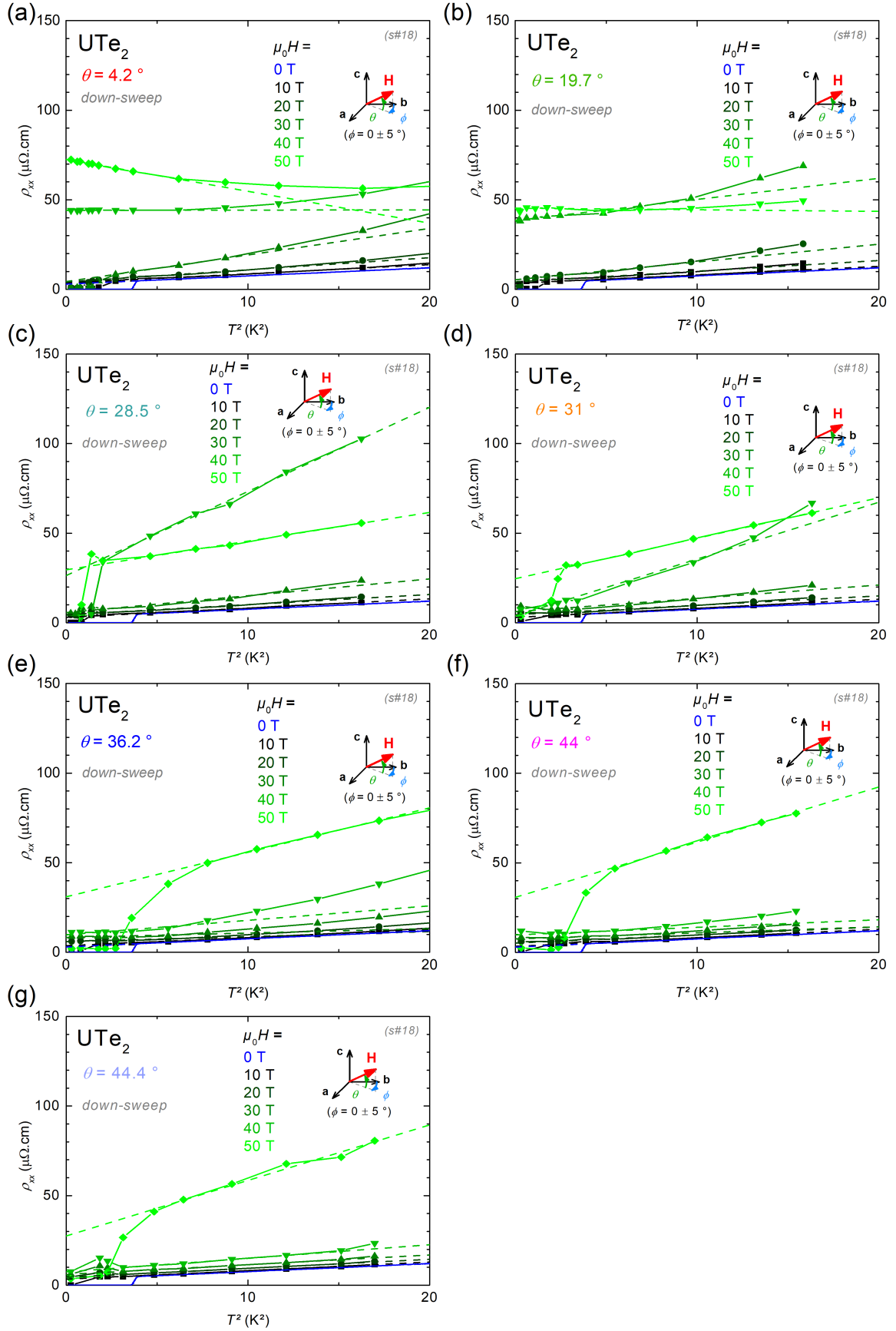


FIG. S8. Electrical resistivity ρ_{xx} versus T^2 of UTe₂ sample #18 at magnetic fields $\mu_0 H = 0, 10, 20, 30, 40$, and 50 T, for $\theta =$ (a) 4.2° , (b) 19.7° , (c) 28.5° , (d) 31° , (e) 36.2° , (f) 44° , and (g) 44.4° . The dashed lines correspond to low- T Fermi-liquid fits by $\rho_{xx} = \rho_0 + AT^2$ in the temperature range $T_{sc}^{\text{nonset}} < T \leq 4.2$ K.

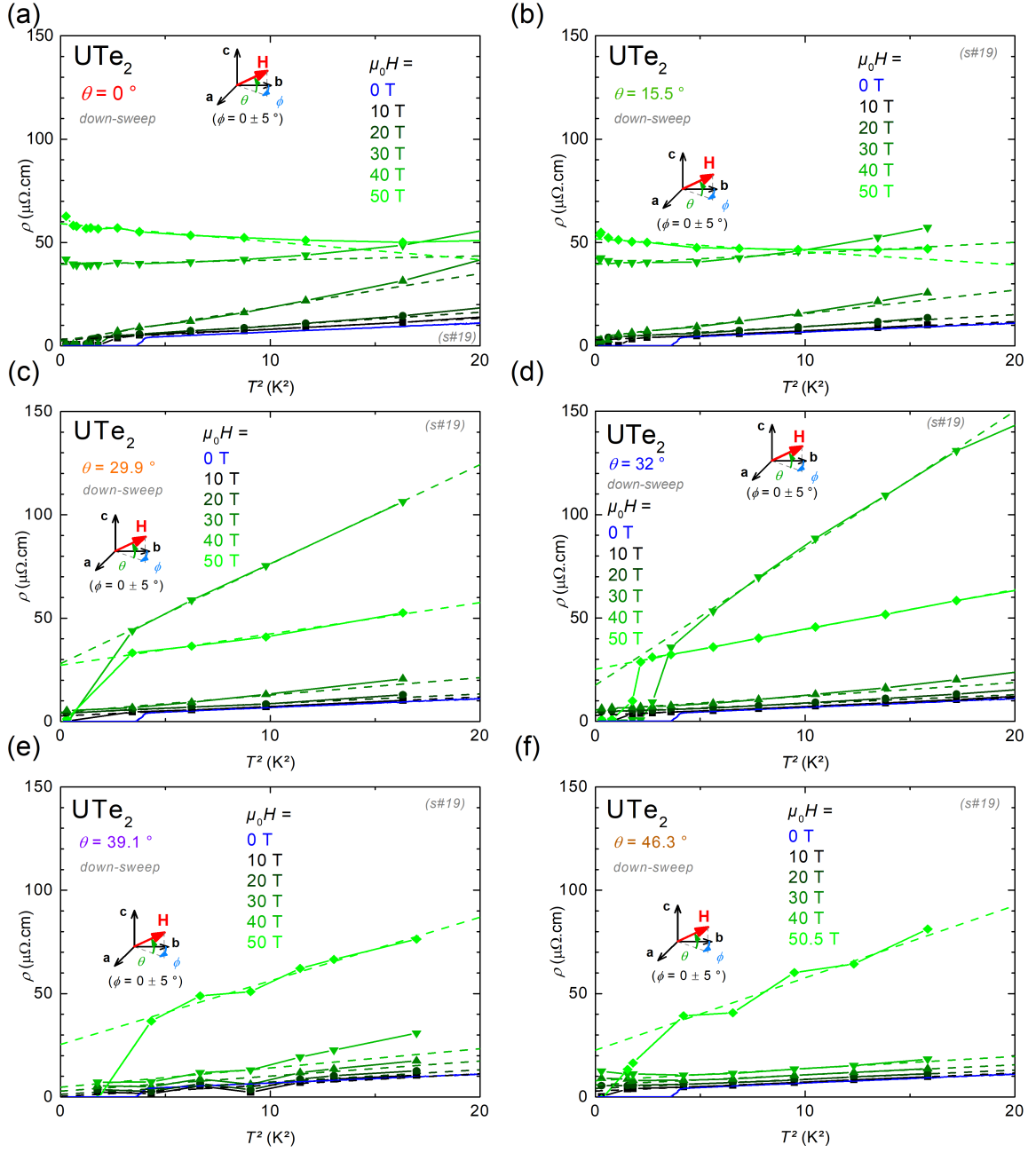


FIG. S9. Electrical resistivity ρ_{xx} versus T^2 of UTe_2 sample #19 at magnetic fields $\mu_0 H = 0, 10, 20, 30, 40$, and 50 T , for $\theta =$ (a) 0° , (b) 15.5° , (c) 29.9° , (d) 32° , (e) 39.1° , and (f) 46.3° . The dashed lines correspond to low- T Fermi-liquid fits by $\rho_{xx} = \rho_0 + AT^2$ in the temperature range $T_{sc}^{onset} < T \leq 4.2 \text{ K}$.

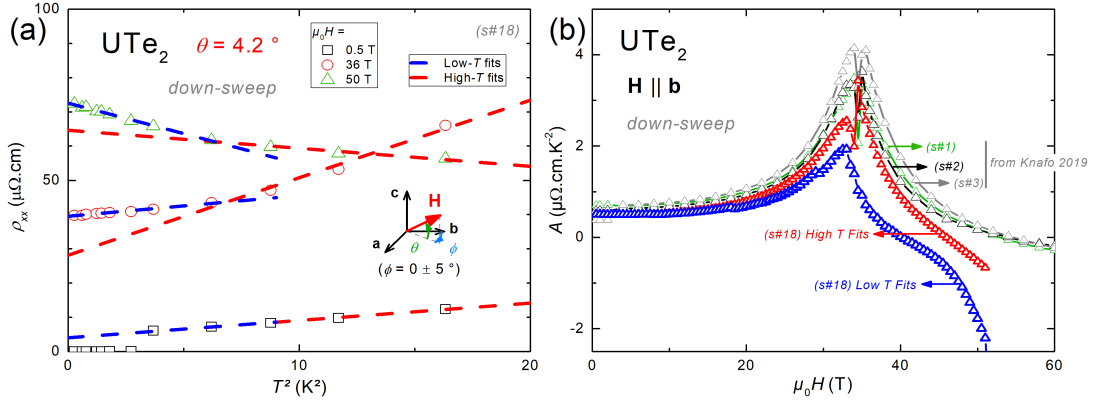


FIG. S10. (a) Electrical resistivity ρ_{xx} versus T^2 of UTe₂ sample #18 at magnetic fields $\mu_0 H = 0.5, 36$, and 50 T, for $\theta = 4.2^\circ$. The blue and red dashed lines correspond to low- T and high- T Fermi-liquid fits by $\rho_{xx} = \rho_0 + AT^2$ in the temperature ranges $T_{sc}^{onset} < T \leq 4.2$ K and 2.1 K $\leq T \leq 4.2$ K, respectively. (b) Magnetic-field dependence of the Fermi-liquid coefficient A extracted for $\mathbf{H} \approx \parallel \mathbf{b}$, on sample #18 grown by the MSF method studied here (low- T and high- T fits) and on samples #1 \rightarrow 3 grown by the CVT method and studied in [S10] (low- T fits).

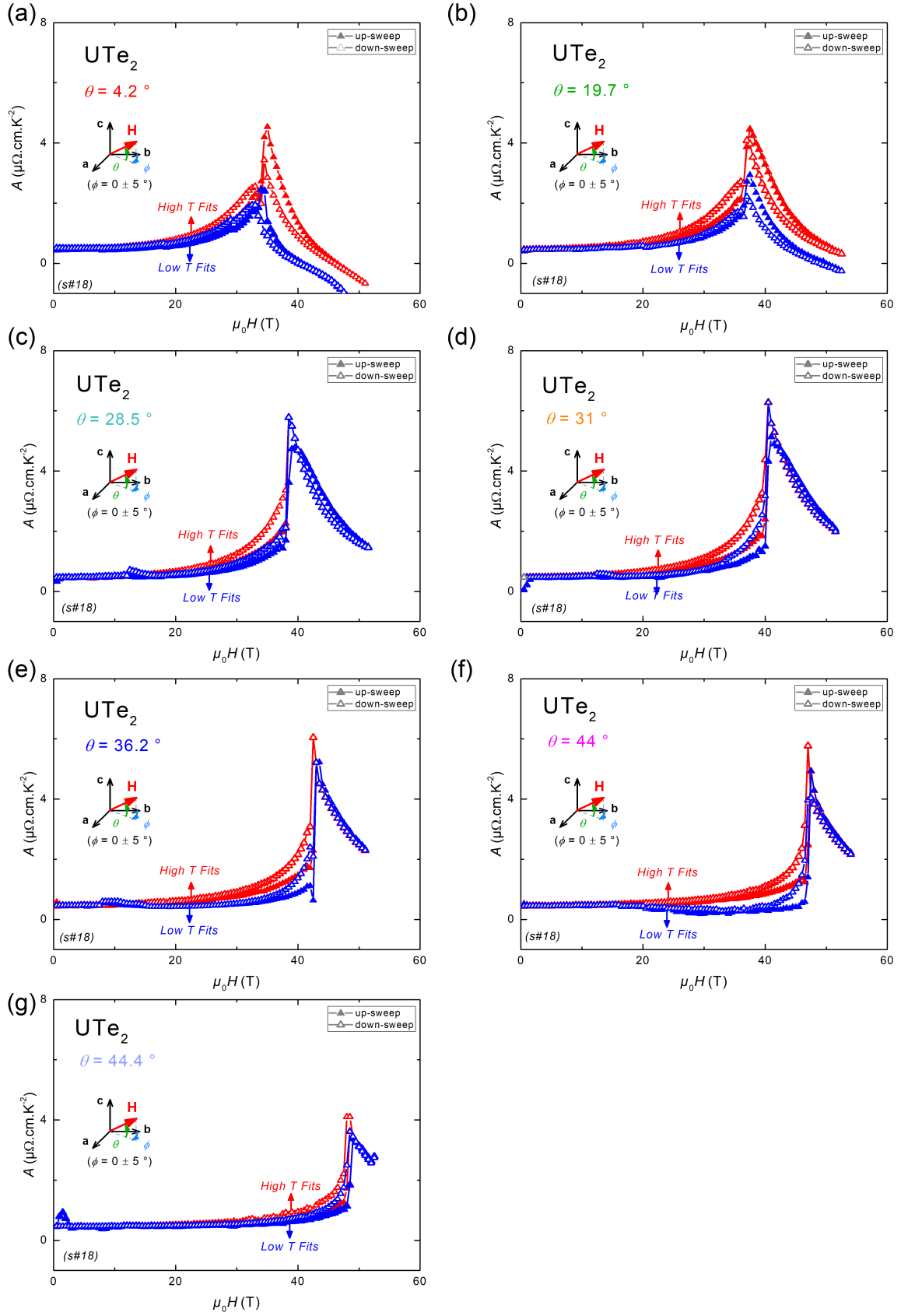


FIG. S11. Magnetic-field variation of the Fermi-liquid coefficient A extracted from low- T and high- T fits of the electrical resistivity ρ_{xx} of UTe₂ sample #18, for $\theta =$ (a) 4.2° , (b) 19.7° , (c) 28.5° , (d) 31° , (e) 36.2° , (f) 44° , and (g) 44.4° . Up- and down-sweep data are represented by closed and open symbols.

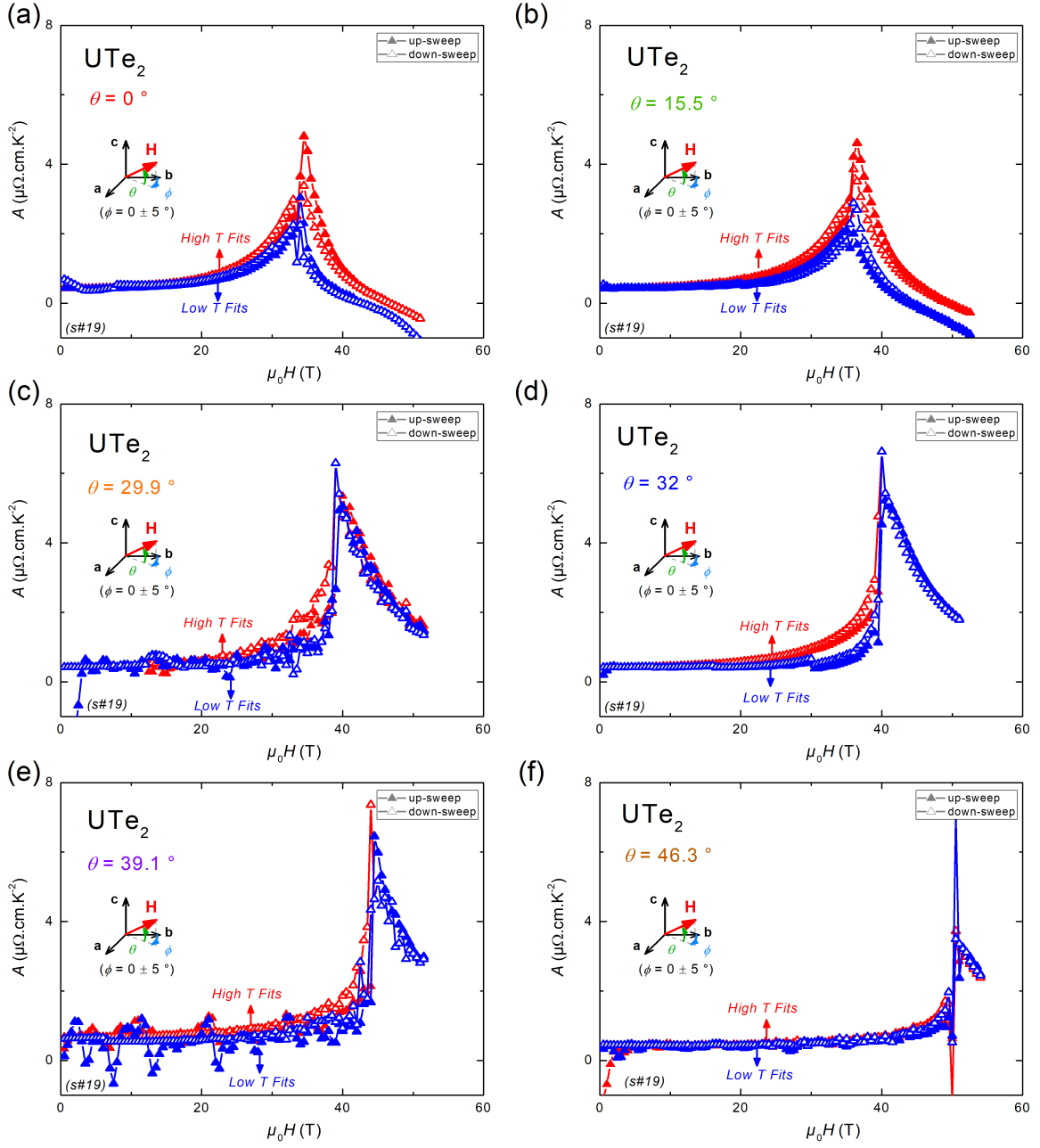


FIG. S12. Magnetic-field variation of the Fermi-liquid coefficient A extracted from low- T and high- T fits of the electrical resistivity ρ_{xx} of UTe_2 sample #18, for $\theta =$ (a) 0° , (b) 15.5° , (c) 29.9° , (d) 32° , (e) 39.1° , and (f) 46.3° .

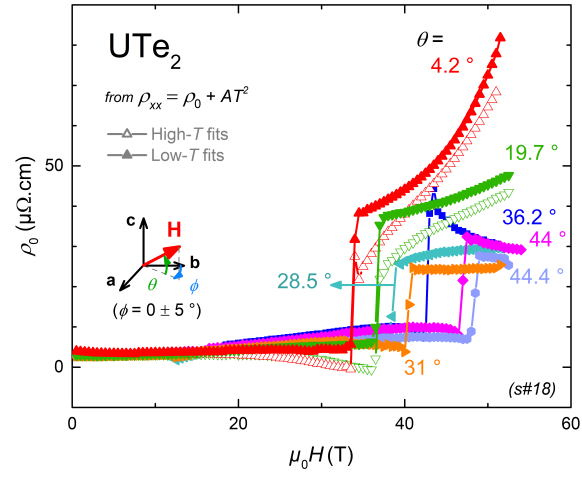


FIG. S13. Magnetic-field variation of the residual resistivity ρ_0 extracted from Fermi-liquid fits to the electrical resistivity of UTe₂ sample #18, for $4.2^\circ \leq \theta \leq 44.4^\circ$.

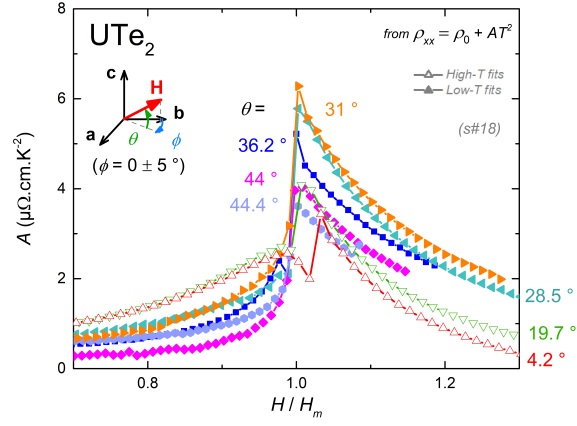


FIG. S14. Variation of the coefficient A extracted from Fermi-liquid fits to the electrical resistivity of UTe₂ sample #18, for $4.2^\circ \leq \theta \leq 44.4^\circ$, from high- T fits for $\theta < 20^\circ$ and low- T fits for $\theta > 20^\circ$, as a function of H/H_m .

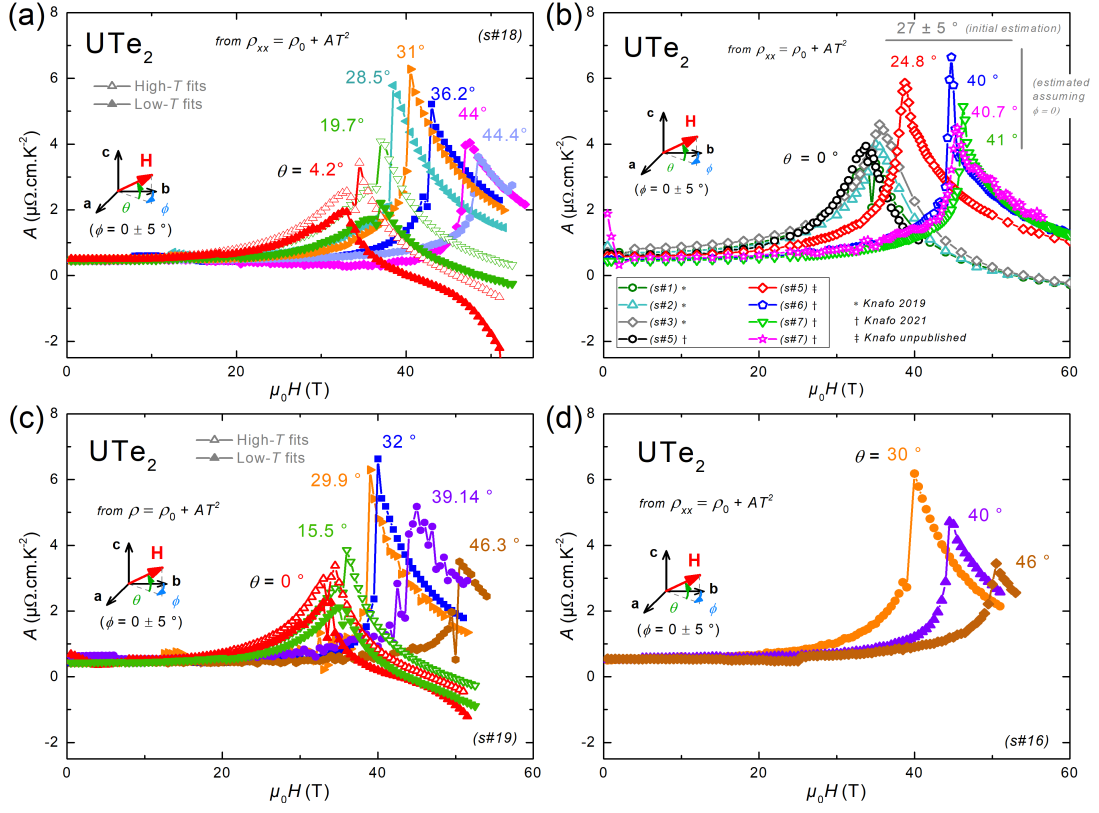


FIG. S15. Magnetic-field variation of A obtained from Fermi-liquid fits to the electrical resistivity ρ_{xx} of (a) sample #18 for $4.2^\circ \leq \theta \leq 44.4^\circ$, (b) samples #1 ($\theta = 0^\circ$), #2 ($\theta = 0^\circ$), #3 ($\theta = 0^\circ$), #5 ($\theta = 0^\circ$ and 24.8°), #6 ($\theta = 40^\circ$), and #7 ($\theta = 40.7^\circ$ and 41°), (c) sample #19 for $0^\circ \leq \theta \leq 46.3^\circ$, and (d) #16 for $30^\circ \leq \theta \leq 46^\circ$. Samples #16, #18, and #19 have been grown by the MSF technique and studied here, and samples #1, #2, #3, #5, #6, and #7 have been grown by the CVT technique and investigated in [S4, S10, S13].

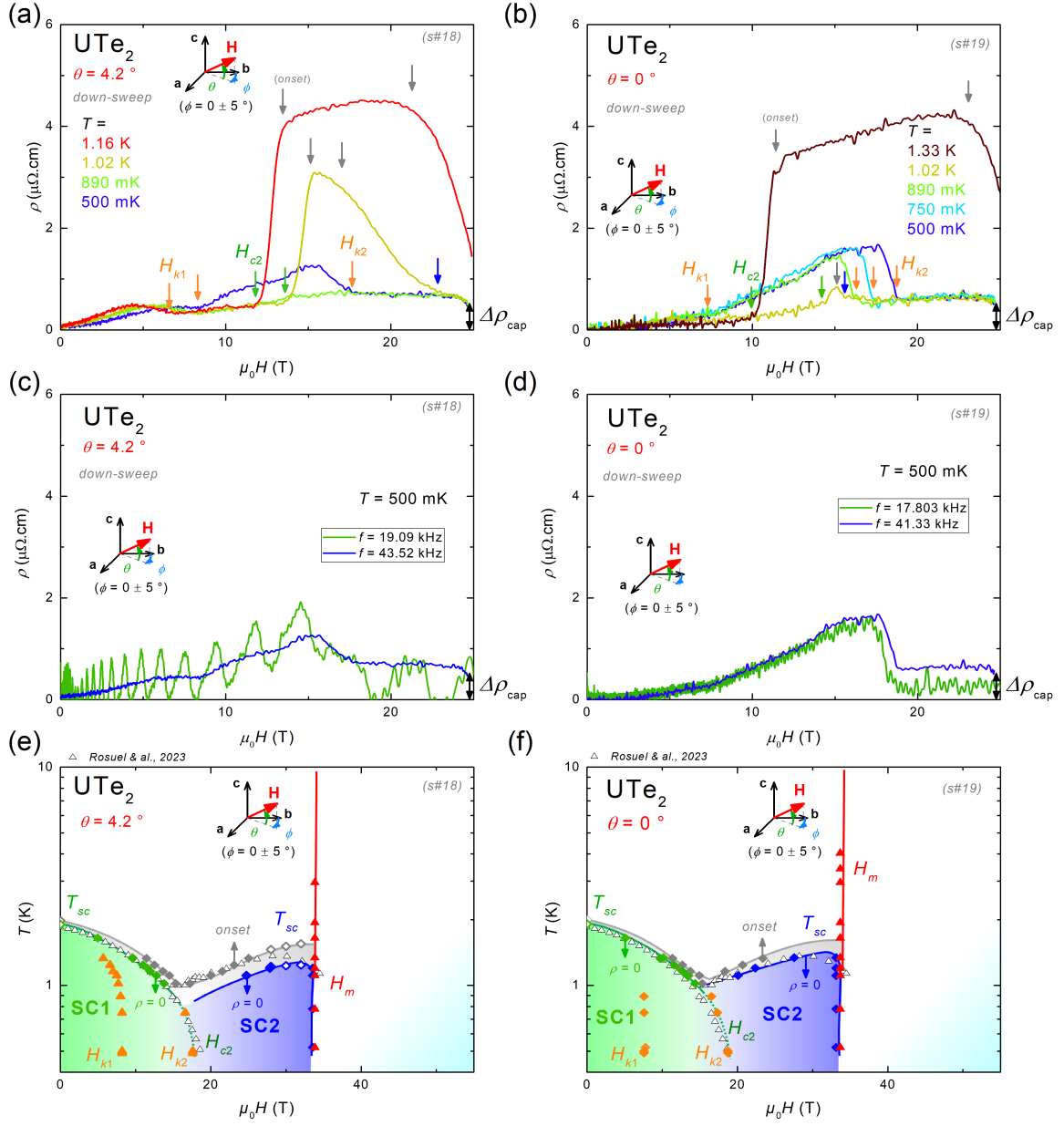


FIG. S16. Electrical resistivity versus magnetic field up to 25 T of (a) sample #18 for $\theta = 4.2^\circ$ at temperatures $500\text{ mK} \leq T \leq 1.16\text{ K}$ and (b) sample #19 for $\theta = 0^\circ$ at temperatures $500\text{ mK} \leq T \leq 1.33\text{ K}$. Comparison of two pulsed-field shots performed at $T = 500\text{ mK}$ on (c) sample #18 for $\theta = 4.2^\circ$, at the current frequencies $f = 19.09$ and 43.52 kHz and (d) sample #19 for $\theta = 0^\circ$, at the current frequencies $f = 17.803$ and 41.33 kHz , showing the presence of a non-intrinsic contribution $\Delta\rho_{\text{cap}} \simeq 0.5\text{ }\mu\Omega$ to the resistivity at 25 T induced by capacitive effects at frequencies $f \simeq 40\text{ kHz}$. Magnetic-field-temperature phase diagrams determined from electrical-resistivity data collected here on (e) sample #18 for $\theta = 4.2^\circ$ and (f) sample #19 for $\theta = 0^\circ$. These phase diagrams include superconducting phase boundaries determined from heat-capacity measurements in [S14].